SANDIA REPORT

SAND2014-0597
Unlimited Release
Printed February 2014

Numerical Implementation of Time-Dependent Density Functional Theory for Extended Systems in Extreme Environments

Andrew D. Baczewski, Luke Shulenburger, Michael P. Desjarlais, Rudolph J. Magyar

Prepared by
Sandia National Laboratories
Albuquerque, New Mexico 87185 and Livermore, California 94550

Sandia National Laboratories is a multi-program laboratory managed and operated by Sandia Corporation, a wholly owned subsidiary of Lockheed Martin Corporation, for the U.S. Department of Energy's National Nuclear Security Administration under contract DE-AC04-94AL85000.

Approved for public release; further dissemination unlimited.

Sandia National Laboratories

Issued by Sandia National Laboratories, operated for the United States Department of Energy by Sandia Corporation.

NOTICE: This report was prepared as an account of work sponsored by an agency of the United States Government. Neither the United States Government, nor any agency thereof, nor any of their employees, nor any of their contractors, subcontractors, or their employees, make any warranty, express or implied, or assume any legal liability or responsibility for the accuracy, completeness, or usefulness of any information, apparatus, product, or process disclosed, or represent that its use would not infringe privately owned rights. Reference herein to any specific commercial product, process, or service by trade name, trademark, manufacturer, or otherwise, does not necessarily constitute or imply its endorsement, recommendation, or favoring by the United States Government, any agency thereof, or any of their contractors or subcontractors. The views and opinions expressed herein do not necessarily state or reflect those of the United States Government, any agency thereof, or any of their contractors.

Printed in the United States of America. This report has been reproduced directly from the best available copy.

Available to DOE and DOE contractors from
U.S. Department of Energy
Office of Scientific and Technical Information
P.O. Box 62
Oak Ridge, TN 37831

Telephone: (865) 576-8401
Facsimile: (865) 576-5728
E-Mail: reports@adonis.osti.gov
Online ordering: http://www.osti.gov/bridge

Available to the public from
U.S. Department of Commerce
National Technical Information Service
5285 Port Royal Rd
Springfield, VA 22161

Telephone: (800) 553-6847
Facsimile: (703) 605-6900
E-Mail: orders@ntis.fedworld.gov
Online ordering: http://www.ntis.gov/help/ordermethods.asp?loc=7-4-0#online

SAND2014-0597
Unlimited Release
Printed February 2014

Numerical Implementation of Time-Dependent Density Functional Theory for Extended Systems in Extreme Environments

Andrew D. Baczewski, Luke Shulenburger, Michael P. Desjarlais, Rudolph J. Magyar

Abstract

In recent years, DFT-MD has been shown to be a useful computational tool for exploring the properties of WDM. These calculations achieve excellent agreement with shock compression experiments, which probe the thermodynamic parameters of the Hugoniot state. New X-ray Thomson Scattering diagnostics promise to deliver independent measurements of electronic density and temperature, as well as structural information in shocked systems. However, they require the development of new levels of theory for computing the associated observables within a DFT framework. The experimentally observable x-ray scattering cross section is related to the electronic density-density response function, which is obtainable using TDDFT - a formally exact extension of conventional DFT that describes electron dynamics and excited states. In order to develop a capability for modeling XRTS data and, more generally, to establish a predictive capability for first principles simulations of matter in extreme conditions, real-time TDDFT with Ehrenfest dynamics has been implemented in an existing PAW code for DFT-MD calculations. The purpose of this report is to record implementation details and benchmarks as the project advances from software development to delivering novel scientific results. Results range from tests that establish the accuracy, efficiency, and scalability of our implementation, to calculations that are verified against accepted results in the literature. Aside from the primary XRTS goal, we identify other more general areas where this new capability will be useful, including stopping power calculations and electron-ion equilibration.

Acknowledgment

This work was funded through the Sandia National Laboratories LDRD office under project 165731 in the Radiation Effects and High Energy Density Science research area. Sandia National Laboratories is a multi-program laboratory managed and operated by Sandia Corporation, a wholly owned subsidiary of Lockheed Martin Corporation, for the U.S. Department of Energys National Nuclear Security Administration under contract DE-AC04-94AL85000.

Contents

Nomenclature **9**

1 First Principles Simulations of Coupled Electron-Ion Dynamics in Warm Dense Matter **11**

X-Ray Thomson Scattering and Coupled Electron-Ion Dynamics 11

Time-Dependent Density Functional Theory at Elevated Temperatures 14

Contents of this Report 16

2 TDDFT in the PAW Formalism **17**

PAW Method 17

Overview of PAW for Standard DFT 17

PAW for the TDKS Equations 19

Overview of Implementation 19

Outline of a TDDFT Calculation 19

Time Integration of the TDKS Equations 20

Parallelism 23

3 Propagation of Stationary States **25**

Problem Statement 25

Results 26

Accuracy Benchmarks 26

Solver Benchmarks 27

Scalability Benchmarks 28

4 Calculation of Optical Response **33**

Problem Statement 33

Results 35

5 Electron-Ion Dynamics and Stopping Power **39**

Ehrenfest-TDDFT 39

Stopping Power 40

6 Conclusion **45**

Summary 45

Future Work 45

References **47**

Appendix

A **51**

A.1 Matrix Elements 51

A.2 Calculation of Bulk Optical Response 53

List of Figures

1.1 An idealization of XRTS data illustrating the characteristic 3 peak structure. 12

3.1 Error in the lowest (top) and highest (bottom) TDKS orbitals as a function of time. Insets: Zooming in on linear growth in global error (top) and illustration of accumulated phase error (bottom). System: 16 Be atoms at 5000K. 29

3.2 Stability of the Hartree energy over thousands of steps for 16 Be atoms initialized at $t = 0$ in the Mermin ground state at 5000K. 30

3.3 Scaling of the time per step with the accuracy guaranteed by the iterative solve. System: 16 Be atoms at 5000K. 30

3.4 Scaling of the number of iterations required to achieve fixed accuracy as a function of the basis set size. System: 16 Be atoms at 5000K. 31

3.5 Strong scaling of the time per step for a WDM system with 30 Xe atoms and 1024 orbitals. 31

3.6 The variation in the time per step in changing the number of orbitals per core for 512 cores with 1024 orbitals in total. The time per step is broken into different stages to highlight the dominant cost being the Crank-Nicolson update. 32

4.1 Dipole absorption spectrum of a sodium dimer. Inset: molecular structure and the ground state charge density. 36

4.2 Dipole absorption spectrum of benzene. Inset: molecular structure and the ground state charge density. 37

4.3 The dipole absorption spectrum of a sodium dimer at finite temperature. Initial conditions are drawn from Mermin DFT calculations at the indicated temperatures. Result are only due to a perturbing field applied along the dimer axis. 38

5.1 Scalability comparison of DFT-MD and Ehrenfest-TDDFT. Both methods are evaluated using the same time step, presenting a simplest-case scenario for DFT-MD. 41

5.2 View along the ⟨100⟩ direction for channeling (left) and off-channeling (right) trajectories. Blue spheres represent Al atoms, while the pink sphere indicates the proton. 42

5.3 Stopping power of a proton in cold Al compared to SRIM/TRIM database and results published in [39]. Channeling ⟨100⟩ and off-channeling trajectories give similar results. 43

5.4 Force acting on proton in the stopping power calculations for channeling and off-channeling trajectories. 43

Nomenclature

AE: All-Electron
DFT: Density Functional Theory
EOS: Equation Of State
KS: Kohn-Sham
MD: Molecular Dynamics
PAW: Projector Augmented Wave
PS: Pseudized
SCF: Self-Consistent Field
TD: Time-Dependent
WDM: Warm Dense Matter
XRTS: X-Ray Thomson Scattering

Unless otherwise indicated, atomic units are used in which $\hbar = e = m_e = \frac{1}{4\pi\epsilon_0} = 1$.

Chapter 1

First Principles Simulations of Coupled Electron-Ion Dynamics in Warm Dense Matter

This report begins with a discussion of the scientific addressed by the methods developed here. In particular, we give a brief overview of experimental X-Ray Thomson Scattering (XRTS) techniques for the characterization of warm dense matter (WDM), and the need for a first principles theoretical description using Time-Dependent Density Functional Theory (TDDFT). A brief discussion is provided of the primary output of the new computational tool, and connections are made to the observables that we seek to characterize. Emphasis is placed on the importance of capturing the elevated temperatures that typify WDM, as well as additional approximations that accompany coupled ion dynamics. Finally, the layout of the report is summarized.

X-Ray Thomson Scattering and Coupled Electron-Ion Dynamics

The last decade has seen a surge of combined computational and diagnostic advances in the WDM regime [1] of the phase diagrams of many materials [1, 2, 3, 4, 5]. This is important because this region is critical to the modeling and understanding of planetary formation [6] and inertial confinement fusion [7]. The connection between materials properties and modeling is through tabulated equation of state (EOS) and constitutive property models that have hitherto been constructed to connect ambient data and plasma physics models with little information in the WDM region.

One of the important scientific needs in WDM is the ability to routinely measure temperatures of shocked materials. A rapidly advancing technology is the use of high intensity x-ray sources to measure the temperature, density, and structure of WDM. Recent advances in XRTS enable its use in measuring structural properties, densities, and temperatures through

[1] WDM regime is loosely defined as solid density matter at temperatures in the eV range and pressures in the MBar range, although the precise definition of this term remains the subject of debate.

features in measured x-ray scattering data [8]. This technique can be used to test EOS models by providing a measure of bulk temperature and density. Figure 1.1 presents an idealization of XRTS data. The asymmetry of the Compton scattering peaks around the central elastic feature is directly related to the electron temperature. XRTS is coming on-line as a diagnostic tool at several shock compression facilities such as LCLS, Omega, DESY, Tsinghua, and Sandia's Z-machine.

The x-ray radiation can be detected at various scattering angles providing information about the electronic and ionic structure of WDM on a time scale commensurate with shock experiments. The back-scattered x-rays resulting from inelastic Compton scattering provide information about the temperature and charge state of the plasma. The forward x-rays are scattered by long-range collective charge density oscillations or plasmons [9]. The measurement of the forward scattered plasmon asymmetry provides a direct measurement of the temperature of visibly opaque plasmas [10]. While the theory and modeling efforts for the former are well established, the latter collective response remains a challenge [9, 11, 12, 13, 14]. The x-ray scattering response is directly related to the dynamic structure factor (DSF) of materials. This can be related to the imaginary part of the dielectric function through the fluctuation dissipation theorem, and consequently, provides a direct route to temperature diagnostics in the collective limit through measurement of the plasmon response.

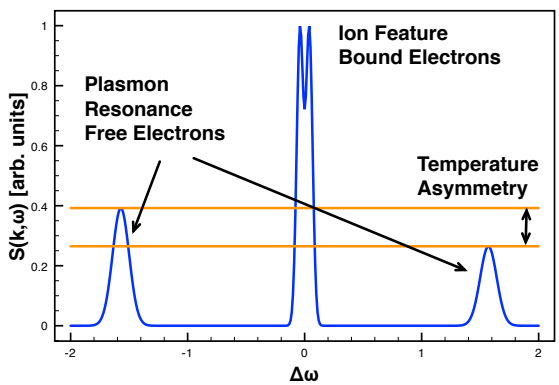

Figure 1.1. An idealization of XRTS data illustrating the characteristic 3 peak structure.

The principle of detailed balance governing the plasmon scattering asymmetry is very general, the in-depth understanding of XRTS data from first principles remains elusive. Results in the non-collective (high-k, Compton limit, short-ranged) are well understood, but the collective limit (low-k, plasmons, long-ranged) is not as well understood. This is because the most accurate models used so far (Chihara) are semi-empirical [15]. In these models, the x-ray response is decomposed into physically intuitive contributions, each treated with varying levels of approximation, that are summed to give a total result. Often, the basic physics described by one element overlaps with other terms. For example, the use of DFT-Molecular Dynamics (MD) based structure factors degrades the accuracy of the summed

results when it is used to replace a simpler model structure factor. A more direct approach would be to calculate the full dynamic structure factor from an explicit simulation of electron and nuclear dynamics. In so far as DFT-MD does not explicitly treat electronic dynamics, a new simulation tool that includes these is needed. Beyond XRTS, such a tool would also be capable of modeling electron-ion energy transfer and would be of great significance to the lab mission.

The spectrally-resolved differential XRTS cross section is directly related to the electronic dynamic structure factor, $S_{ee}(\mathbf{k},\omega)$, through

$$\frac{d^2\sigma}{d\Omega d\omega} = {\sigma_T}^2 \sqrt{\frac{E_f}{E_i}} S_{ee}(\mathbf{k},\omega). \tag{1.1}$$

Here, $\sigma_T = \frac{8\pi}{3}\left(\frac{e^2}{4\pi\epsilon_0 mc^2}\right)^2$ is the Thomson scattering cross section, and E_i and E_f are the energies of the incident and scattered photons. The dynamic structure factor is then related to the system response function, $\chi_{ee}(\mathbf{k},\omega)$, using the Fluctuation-Dissipation Theorem:

$$S_{ee}(\mathbf{k},\omega) = \frac{\hbar}{\pi n_e} \frac{\Im\chi_{ee}(\mathbf{k},\omega)}{1-\exp(-\beta_e\hbar\omega)}. \tag{1.2}$$

Here, n_e is the number density of electrons and β_e is the inverse thermal energy of the electrons. This relationship provides us with a means of using XRTS data to access a quantity of relevance to many-body theory that can be computed within TDDFT.

The DSF is from the direct space-time Fourier transform of the density operator correlation function:

$$S_{ee}(\mathbf{k},\omega) = \frac{1}{2\pi}\int d\mathbf{r}dt \exp(i\omega t - i\mathbf{k}\cdot\mathbf{r})\frac{1}{N}\langle\int d\mathbf{r}'\hat{n}(\mathbf{r}+\mathbf{r}',t)\hat{n}(\mathbf{r}',0)\rangle. \tag{1.3}$$

Since there is no obvious way to define the density operator as a functional of the density, we need to relate the correlation function to a physical TD response of the system. Such a response can be obtained by following the real-time dynamics of the system after an impulsive potential is applied. The DSF can be found over a large range of k by decomposing the exciting field into a set of fixed perturbations of the form $v_{pert}(\mathbf{r},t) = I_0\delta(t)\ e^{i\mathbf{k}\cdot\mathbf{r}}$ [16] with I_0 an arbitrarily small perturbation and $\mathbf{k}$ a wave-vector commensurate with the super cell. The scale of $\mathbf{k}$ is determined by the reciprocal lattice spacing of the super-cell, and a larger super-cell allows us to simulate ever smaller $\mathbf{k}$'s. For each $\mathbf{k}$, we can find the response of the system by integrating the equations of motion and recording the density response. The DSF is related to the Fourier transform from time to frequency domain of the density response,

$$S_{ee}(\mathbf{k},\omega) = -\frac{1}{\pi I_0}\Delta n(\mathbf{k},\omega). \tag{1.4}$$

While this implementation does not require the use of the vector potential it will not directly provide information about the $\mathbf{k}\to 0$ limit. There exist schemes, that we will discuss later, that allow the calculation of $\epsilon^{-1}(0,\omega)$ granting us access to this limit.

In this report, we detail our efforts to develop a tool to model WDM by applying the machinery of TDDFT to extended systems. In TDDFT, the electron wave-functions are allowed to freely evolve in time and to simultaneously affect the ionic dynamics. X-rays can be modeled as classical fields perturbing a super-cell of atoms and nuclei in real time. Material properties can be extracted through the analysis of time-evolving quantities such as the TD dipole moment. This modeling approach introduces several theoretical and numerical challenges, several of which we have overcome and will describe in this report. In what follows, we aim to:

1. Demonstrate the computational advances achieved in implementing a real-time electron dynamics capability in a Projector Augmented Wave (PAW) code for extended systems.
2. Give some indication that our implementation is numerically sound, efficient, and scalable.
3. Validate this tool by comparing to results for cold systems that have been presented in the scientific literature.
4. Discuss our strategy for extending TDDFT to nonzero temperatures and compressed densities.

Having established the validity of our implementation in this report, we will discuss the subsequent scientific challenges that will arise as the focus of this project shifts from programming to fundamental science. Immediate extensions of the capability developed herein will be be to compare x-ray responses computed via TDDFT with Kubo-Greenwood results from the literature. Soon after, fully coupled WDM electron-ion dynamics will be explored, and some indication will be given as to how this capability is being implemented and tested.

Time-Dependent Density Functional Theory at Elevated Temperatures

TDDFT is a computational framework to simulate dynamics of a quantum many-body system by considering an auxiliary non-interacting system in an effective local potential. The advantage of such a paradigm is that the memory required to store the state of the auxiliary system and the computational processing time required to time evolve it is significantly less than for a generic many-body wave-function or even a Green's function. The trade off is that now the equation of motion for the non-interacting system is highly non-linear and the effective potential must be approximated. The fundamentals of the theory are established by the Runge-Gross theorem [17] and subsequently formalized by Baerends and others who showed that given a density that is time evolved for a given internal interaction type, there exists at most one local multiplicative potential that would give the time evolution of that density according to a Schrödinger-like equation of motion [17]. This formalism has been generalized to TD ensembles [18, 19].

TDDFT provides a convenient framework to describe the many particle interacting electron dynamics. In the KS orbital picture, we evolve a set of KS orbitals under the action of

the time-dependent Kohn-Sham equations:

$$i\frac{d}{dt}|\psi_n(t)\rangle = \mathcal{H}_{KS}(t)|\psi_n(t)\rangle \tag{1.5}$$

Here, $|\psi_n(t)\rangle$ is the nth KS orbital and $\mathcal{H}_{KS}$ is the KS Hamiltonian, $\mathcal{H}_{KS} = -\frac{\nabla^2}{2} + v_{ext}(\mathbf{r}) + v_H(\mathbf{r}) + v_{XC}[n(\mathbf{r},t), \Psi(0), \Phi(0)](\mathbf{r})$. The density is obtained via $n(\mathbf{r},t) = \sum_n f_n|\psi_n(\mathbf{r},t)|^2$. The first term on the right describes the kinetic energy, the next is the nuclear Coulomb potential plus external perturbations, followed by the classical Hartree potential, and finally the exchange-correlation potential. In addition to the time-varying many-electron density, the potential in TDDFT depends on the initial many-body state and the choice of initial KS representation. The last term is typically approximated in TDDFT and subsumes the many-body effects not included in the former terms and depends on the time-dependent density, the initial many-body wave-function, and the initial KS representation of the initial state. Most practical functionals include only the dependence on the time-varying density.

The primary focus of this report is the implementation of TDDFT time evolution into an existing PAW electronic structure code, VASP 5.3.3 [20, 21, 22]. There are three major theoretical challenges in simulating extended systems within TDDFT. First, a computational engine must be constructed to time-evolve the TDKS equations (Equation 1.5). Second, a physically reasonable initial state must be chosen that will deliver relevant physics under the TDKS evolution. Since the KS orbitals do not in general represent physical quantities, the initial state must be presented as a physical initial charge distribution and mapped back unto the KS orbitals. Third is time-dependent potential energy surface hopping.

The initial state is chosen as a weighted set of KS orbitals reproducing the ensemble density of the desired hot thermalized electrons. We point out that we are using fractional weights to model a density that is derived from an ensemble of solutions. Mermin DFT reproduces the results of a grand canonical solution through the use of a fractionally weighted orbital set that provides the density of electrons at elevated temperature. TDDFT on the other hand, time evolves an initial density to a final one. The functional that would be required to time-evolve a warm electron density to another non-equilibrium density is a different functional than would be used for a typical optical response simulation of a ground state density through initial state dependence. However, as a first approximation we use adiabatic semi-local ground-state zero temperature approximations to the KS potential. It has been suggested that non adiabatic electron-electron effects are less important at higher densities and for lower Z scattered particles [23], and so are less likely to contribute in WDM. As an initial state approximation, we will start our TDDFT simulations with a weighted set of orthogonal orbitals that reproduce a Mermin finite temperature DFT density. Here, the orbital occupations are allowed to range from 0 to 1. The choice of partial occupancies is theoretically sound within the original Runge-Gross formulation, and is naturally compatible with the Mermin elevated temperature potential. The approximation and development of improved models for the effective local potential and in particular, the exchange-correlation contribution, is an active area of research. For the rest of this report, we will restrict ourselves to adiabatic local and semi-local functionals.

The second approximation beyond just the use of TDDFT is the way in which nuclear

motion is coupled to the electronic motion. The nuclei are moved according to Hellman-Feynman forces in the potential energy surface created by the time-evolved electrons. The resulting dynamics, Ehrenfest dynamics, do not describe non-adiabatic effects where multiple potential energy surfaces have similar energy affecting the dynamics through non-Ehrenfest impulses on the nuclei caused by potential energy surface hops by the electrons. At elevated temperatures, we expect many potential energy surfaces to come into play, and in future work, we will develop schemes to handle many surface hops through dynamically changing the occupation of the KS orbitals.

Several challenges are that the positions of the level crossings are not necessarily well-reproduced by KS eigenvalues or DFT total energies as excited state surfaces are not guaranteed to exist. Additionally, the state we are propagating represents an ensemble of states that should reproduce a density that would result from an ensemble of solutions. There is no fundamental relationship between the spectrum of this system and the physical system.

The range of capabilities of the methods described here includes the conditions most important to the dynamic interaction of x-rays and WDM. It is important to recognize the length scales of these processes and to compare these to the potential capabilities of our computer simulation. The interaction time between electrons and the duration of our perturbing x-ray pulse is on the order of femtoseconds (10^{-15} sec). The time step of electronic propagation is on the order of attoseconds (10^{-18} sec). Nuclear motion is on the order of picoseconds (10^{-12}). The plasma time scale is about 200 fs and represents the time scale beyond which we expect linear response features to appear. The size of the super-cells is on the order of 10 Å on a side. The wavelength of typical x-ray pulses are between 0.1 and 10 Å. Typical super cells contain on the order of hundreds of atoms allowing the treatment of many crystal structures of interest and locally disordered systems.

Contents of this Report

The remainder of this report will be concerned with details of extending an existing PAW code to model real-time TDDFT with coupled-ion motion. The VASP code was chosen because of our extensive experience with it and its well-tested PAW library. The following is a chapter-by-chapter outline of the specific contents:

- Details of the PAW method as applied to the TDKS problem (Chapter 2).
- Benchmarks for the evolution of a stationary KS ground state (Chapter 3).
- Calculation of the optical response of finite and extended systems (Chapter 4).
- Application of electron-ion dynamics to stopping power calculation (Chapter 5).

With the exception of Chapter 2, each chapter will be concerned with the development of a particular capability in our real-time TDDFT implementation. These chapters will first present a mathematical statement of the type of calculation being enabled, and then follow up with implementation details and validating results.

Chapter 2

TDDFT in the PAW Formalism

In this chapter, we introduce details and notations germane to our integration of real-time TDDFT into an existing electronic structure package. In particular, we focus on the PAW method that is used to efficiently treat the all-electron (AE) problem in extended systems, and its extension to real-time TDDFT.

PAW Method

Overview of PAW for Standard DFT

The PAW method was first developed by Blöchl [24] as a generalization of pseudopotential methods. It is closely related to the ultrasoft pseudopotential method of Vanderbilt [22, 25, 26], though it retains an explicit connection to the AE problem. Simply put, it is an especially efficient means of performing electronic structure calculations using a plane wave basis. In discussing the details of this method, we utilize a notation similar to the ones used in [22] and [24] - namely, we will refer to AE and pseudized (PS) objects, with the latter being indicated by the presence of a tilde ($\sim$).

The crux of the PAW method is the assertion that the AE and PS orbitals can be related via a simple linear transformation:

$$|\psi_n\rangle = \mathcal{T}|\tilde{\psi}_n\rangle = |\tilde{\psi}_n\rangle + \sum_I \sum_j \left(|\phi_j^I\rangle - |\tilde{\phi}_j^I\rangle\right) \langle \tilde{p}_j^I|\tilde{\psi}_n\rangle \tag{2.1}$$

Here the summation index I taken over each ion in the system, and j is taken over a set of reference states localized to the Ith ion. Here, $|\phi_j^I\rangle$ and $|\tilde{\phi}_j^I\rangle$ are called the AE and PS partial waves, $|\tilde{p}_j^I\rangle$ are called the projectors, and the coefficients of $|\tilde{\psi}_n\rangle$ in a plane wave basis will become our variational quantities. The partial waves are defined such that the AE and PS quantities only differ inside of a compact spherical region about each ion called the augmentation region. In other words, $\mathcal{T}$ reduces to the identity outside of augmentation regions. Further, the projectors are defined such that they are dual to the PS partial waves, $\langle \tilde{p}_{j_1}^I|\tilde{\phi}_{j_2}^I\rangle = \delta_{j_1 j_2}$. The actual construction of these quantities is largely irrelevant to our implementation of real-time TDDFT, and further details can be found in [22]. Of greater

relevance is the manner in which the PAW method modifies the structure of the equations common to the KS formulation of DFT and TDDFT.

The stationary KS problem takes the form of a standard eigenvalue problem at each SCF step - find pairs $\epsilon_n \in \mathbb{R}$ and $|\psi_n\rangle \in L^2$ such that:

$$\mathcal{H}_{KS}|\psi_n\rangle = \epsilon_n|\psi_n\rangle \tag{2.2a}$$
$$\langle\psi_m|\psi_n\rangle = \delta_{mn} \tag{2.2b}$$

This form is the solution of a variational problem, wherein one finds the stationary points of a total energy functional with respect to variations in the coefficients of $|\psi_n\rangle$, subject to the constraint that the solutions be normalized with respect to the L^2 norm. Orthogonality is ensured by the Hermiticity of $\mathcal{H}_{KS}$. In the PAW method, the problem is slightly more complex because the variational degrees of freedom are taken as the PS coefficients, rather than the AE coefficients of relevance to Equation 2.2. Solutions to the PAW variational problem satisfy:

$$\tilde{\mathcal{H}}_{KS}|\tilde{\psi}_n\rangle = \epsilon_n\mathcal{S}|\tilde{\psi}_n\rangle \tag{2.3a}$$
$$\langle\tilde{\psi}_m|\mathcal{S}|\tilde{\psi}_n\rangle = \delta_{mn} \tag{2.3b}$$
$$\tilde{\mathcal{H}}_{KS} = \mathcal{T}^\dagger\mathcal{H}_{KS}\mathcal{T} \text{ and } \mathcal{S} = \mathcal{T}^\dagger\mathcal{T} \tag{2.3c}$$

Rather than a standard eigenvalue problem, we are now met with a generalized eigenvalue problem - find pairs $\epsilon_n \in \mathbb{R}$ and $|\tilde{\psi}_n\rangle \in L^2$ that are no longer orthonormal in the L^2 norm, but a weighted L^2 norm defined in terms of the PAW overlap operator, $\mathcal{S}$.

One of the primary functions of any PAW code is the solution of Equation 2.3 for a fixed $\tilde{\mathcal{H}}_{KS}$ and $\mathcal{S}$. In a conventional DFT calculation this eigenproblem is solved for many different KS Hamiltonians, until a self-consistent solution is achieved, at which point the results can be post-processed. Our implementation of real-time TDDFT will take advantage of this functionality in the following respects:

- Initial conditions for our time evolution will be taken from a conventional fully-converged Mermin DFT calculation.
- Solution of the TDKS equations will require the efficient application of both $\tilde{\mathcal{H}}_{KS}$ and $\mathcal{S}$ to PS kets. The subroutines that perform these operations will be a starting point towards this end.

With this in mind, the form of the TDKS problem will still change considerably. Instead of solving a generalized eigenvalue problem, we will be concerned with time evolving a nonlinear PDE whose initial conditions are drawn from a conventional DFT calculation. In the next section, a proper statement of this problem is given.

PAW for the TDKS Equations

Recalling the form of the TDKS equations in Equation 1.5, we are interested in resolving $|\psi_n(t)\rangle$ that satisfies the following for $t \geq 0$:

$$i\frac{d}{dt}|\psi_n(t)\rangle = \mathcal{H}_{KS}|\psi_n(t)\rangle \tag{2.4a}$$

$$|\psi_n(t=0)\rangle = |\psi_n^0\rangle \tag{2.4b}$$

As with the standard KS equations, when using the PAW method, this form of the problem requires modification, as we are instead interested in working with PS quantities. To arrive at the PAW form of the problem, we simply state that the TD AE and PS orbitals have the same relationship as in a conventional calculation, and then multiply both sides by $\mathcal{T}^\dagger$ for convenience. This yields the following:

$$\mathcal{T}^\dagger i\frac{d}{dt}\mathcal{T}|\tilde{\psi}_n(t)\rangle = \tilde{\mathcal{H}}_{KS}|\tilde{\psi}_n(t)\rangle \tag{2.5}$$

In the presence of ionic motion, the $\hat{T}$ operator will pick up a time-dependence, and we must be careful to include this in the dynamics. Applying the product rule for differentiation on the LHS, we can arrive at an alternative form of the problem:

$$i\mathcal{S}\frac{\partial}{\partial t}|\tilde{\psi}_n\rangle = \left[\tilde{\mathcal{H}}_{KS} + \mathcal{P}\right]|\tilde{\psi}_n(t)\rangle \tag{2.6a}$$

$$\mathcal{P} = -i\mathcal{T}^\dagger\frac{d\mathcal{T}}{dt} \tag{2.6b}$$

In the limit that the ionic degrees of freedom are immobile, $\mathcal{P}$ will vanish, yielding a form of the problem that is at least superficially simpler than Equation 2.5. Chapters 3 and 4 will discuss the solution of Equation 2.6 in the immobile ion limit, for different initial conditions and using different forms of $\tilde{\mathcal{H}}_{KS}$. In Chapter 5, this restriction will be lifted in the context of stopping power calculations in which ionic motion is essential.

Overview of Implementation

In the following subsections, details are provided that describe our implementation of real-time TDDFT. First, an outline of the necessary inputs is provided. Then, the issue of numerical time integration is briefly discussed. Finally, some of the details associated with achieving scalability on distributed memory parallel platforms are discussed.

Outline of a TDDFT Calculation

A real-time TDDFT calculation consists of the following three steps:

1. A preliminary standard DFT calculation that provides a set of KS orbitals for the initial conditions.
2. Propagation of the initial state via the TDKS equations, and the recording of observables.
3. Post-processing of observables to extract physically meaningful information.

Step 1 is accomplished using the established capability of the PAW code to calculate the KS orbitals and weights within the Mermin DFT formalism. This information is written to disk, from which it can be read on subsequent runs. Step 2 is where the majority of our extensions become relevant. The data written in the previous step is read in, and our code constructs physically interesting initial conditions for the TDKS equations. Then, the TDKS equations are numerically integrated, the details of which will be discussed in the next subsection and in Chapter 3. At each time step of the numerical integration, observable quantities are recorded to disk in anticipation of Step 3. Step 3 involves stand-alone scripts and software. For example, in Chapter 4 the optical response of molecular systems will be discussed. Here, the dipole moment of the molecule is stored at each time step, and Step 3 consists of extracting information from the Fourier spectrum of this information.

Among these steps, the most demanding is Step 2. The propagation of the TDKS equations consists of a step-by-step numerical integration, wherein each time step requires the repeated iteration of the following sequence of computations:

1. Construction of the local potential - terms in $\tilde{\mathcal{H}}_{KS}$ that act locally on each KS orbital.
2. Construction of the PAW operators - terms in $\tilde{\mathcal{H}}_{KS}$ and $\mathcal{S}$, that act non-locally on each KS orbital.
3. Solution of a discrete form of the TDKS equations for a single time step.
4. Calculation of the charge density from the updated TDKS orbitals.

Implementing this sequence constitutes the primary technical challenge of this work. However, much of the functionality required can be re-purposed from the extant PAW code, which performs the same steps in seeking a self-consistent solution, albeit with a different way of updating the orbitals in Step 3. With this in mind, we will focus primarily on the numerical integration of the TDKS equations in terms of both the integration scheme itself, and implementation details such as exploiting parallelism. The remaining two subsections discuss these challenges.

Time Integration of the TDKS Equations

Numerical integration of the TDKS equations is a difficult problem, given their inherent nonlinearity. To this end, it is useful to consider the properties of 'good' time integrators, as well as the formal issues that must be addressed in satisfying them. The particular properties of interest are:

- **Unitarity:** That the KS orbitals remain orthonormal throughout the time integration is desirable, as it is a property of the exact solution that can be satisfied in a numerically

exact manner. Physically, this is related to the conservation of charge.

- **Systematically improvable error:** By decreasing the size of the discrete time step, 'better' results are achieved at a particular rate. We are careful to note that this is only with respect to numerical error in the time propagation, and not error in the functional which still exists even with a numerically exact time integration.
- **Long-term stability:** As the end goal is to resolve dynamics on the scale of 100s of fs to a ps, while the electronic time step is on the order of 1 as, having some indication that the chosen integrator is stable is important.

These properties have been listed in order of increasing difficulty in rigorously satisfying them. The construction of unitary time integrators is relatively straightforward, and a number of exemplary methods exist in the literature [27, 28, 29, 30], perhaps the simplest of which is the Crank-Nicolson (or implicit midpoint) method. That unitarity can be guaranteed in spite of the nonlinearity of the TDKS equations is a consequence of the Hermiticity of the TDKS Hamiltonian.

Even so, error estimates for the TDKS equations are more difficult to construct, as the Hamiltonian is an unbounded operator. To this end, in spite of the fact that convergence rates are frequently cited in the literature [30, 31], there are not many rigorous estimates, though some exist[32]. Even so, these estimates are essentially useful for linear problems in quantum dynamics, so within TDDFT they are only valid for isolated cases like stationary states in which the nonlinearity is effectively removed, as will be discussed in Chapter 3. As a rigorous notion of the stability of the TDKS equations is an open problem, benchmarking against these isolated cases is an acceptable limitation, and is among the only rigorous means of testing a TDDFT implementation.

Stability is perhaps the most difficult condition to satisfy, as a consequence of nonlinearity. Even in the analytic case, stability is an open problem taken in the following sense: given a density in a neighborhood of the 'correct' density, at what rate does the difference between the nearby and 'correct' densities increase, if at all? To this end, it is most difficult to find a numerical integrator that is stable, as it is unknown whether or not one can exist. Again, we will start by considering isolated cases like stationary states as a first indication of the correctness of our implementation.

While investigation into other integration schemes is ongoing, so far we have found a great deal of success using the Crank-Nicolson method. This framework requires the solution of the following linear system in updating the KS orbitals from time t to time $t + \Delta t$:

$$\left[\mathcal{S} + \frac{i\Delta t}{2}\tilde{\mathcal{H}}_{KS}(t)\right] |\tilde{\psi}_n(t + \Delta t)\rangle = \left[\mathcal{S} - \frac{i\Delta t}{2}\tilde{\mathcal{H}}_{KS}(t)\right] |\tilde{\psi}_n(t)\rangle \tag{2.7}$$

This particular flavor of the Crank-Nicolson method is typically cited as being first order accurate [31], unless $\tilde{\mathcal{H}}_{KS}$ is a constant in time. To achieve a higher order of accuracy, a predictor-corrector framework is needed. This is achieved in practice using a three-step process:

1. The orbitals at $t + \Delta t$ are estimated using $\tilde{\mathcal{H}}_{KS}$ at time t.

2. An estimate of $\tilde{\mathcal{H}}_{KS}$ at time $t + \Delta t$ is constructed using the 'predicted' orbitals.
3. A 'corrected' $\tilde{\mathcal{H}}_{KS}$ is built from the average of the two Hamiltonians, and used to update the initial orbitals from time t to $t + \Delta t$.

While both flavors of Crank-Nicolson have been implemented, there is little practical difference between the two for the stationary ion problems that we have studied so far. However, we anticipate that the predictor-corrector extension may prove to be significantly more robust when the ions are allowed to move in a more general setting than discussed in Chapter 5.

One implementation concern that arises in using the Crank-Nicolson method is that it is an implicit integrator, and requires the solution of a linear system of equations at each time step. While explicit integrators have been studied, their adoption is somewhat recent [33], and they do not guarantee unitary evolution. In principle, this may be a significant limitation as the unitarity of the exact time propagator guarantees charge conservation. Consequently, we deem the required linear algebra an acceptable cost to accrue.

Given the structure of the PAW Hamiltonian, and the regularity of the plane wave basis, we can achieve an efficient solution of the Crank-Nicolson update equations using an iterative solver. The particular solver that we have implemented is the conjugate gradient squared (CGS) method, first introduced in [34] for the solution of sparse non-symmetric systems. The computational cost of this solver, at each time step, scales as $\mathcal{O}(N_{it} N_b N_{pw}^{\alpha} \log^{\beta} N_{pw})$. The various factors in this cost are defined as:

- N_{it}**:** the number of iterations required to achieve a desired residual.
- N_b**:** the number of KS orbitals being considered in the calculation.
- $N_{pw}^{\alpha} \log^{\beta}(N_{pw})$**:** the cost of performing a matrix-vector product between the the operator on the left hand side of Equation 2.7 and a trial ket. Here, N_{pw} is the size of the plane wave basis in which the ket is given, and α and β are parameters that depend upon the manner in which the product is effected.

It is evident that explicitly forming the LHS operator in Equation 2.7 and applying the matrix-vector product directly will yield $\alpha = 2$ and $\beta = 0$, the cost of a dense matrix-vector multiplication. However, a judicious use of FFTs can lead to a cost complexity with $\alpha = 1$ and $\beta = 1$. Considering each term of the KS Hamiltonian, FFTs are used as follows:

- **Kinetic energy:** This term is diagonal in the basis of plane waves, and does not require the use of an FFT.
- **Local potential:** An FFT maps the plane wave coefficients onto a real-space grid, on which the local potential term is diagonal. It is applied, and an IFFT is used to get the coefficients of the product in the plane wave basis.
- **Nonlocal potential:** In principle, these terms can be computed in either the plane wave or real-space basis. In either case, the compactness of the augmentation region keeps the operation sparse.

In terms of the number of electrons (N_e) in the system, N_{pw} and N_b scale linearly, while N_{it} is empirically insensitive to system size. Consequently, the cost of a TDDFT

evolution scales as $\mathcal{O}(N_e^2 \log(N_e))$, in contrast to the dominant $\mathcal{O}(N_e^3)$ cost of a conventional DFT calculation, in which orthogonalization is the dominant cost. Of course, the TDDFT evolution begins from an orthogonalized set of orbitals, so this cost is still implicit in some capacity. Benchmarks for the performance of this integrator will be presented in the Results Section of Chapter 3.

Parallelism

Three flavors of hierarchical parallelism are available in VASP 5.3.3. Data and work can be distributed over both orbitals and plane wave coefficients, and work can be distributed over independent points in the Brillouin Zone for extended systems. In practice, because WDM systems require a large number of orbitals to be included due to the significant smearing of the Fermi-Dirac distribution, and as these systems will have a low degree of long-range order, parallelism over orbitals should be weighted most heavily. This is further compounded by the fact that, unlike in conventional DFT-MD, there is no orthogonalization of the KS orbitals at each step. With this in mind, because the update of the KS orbitals is the dominant cost in each time step, and because it can be achieved independent of all other bands, this makes parallelism in TDDFT somewhat easier to achieve than in conventional DFT. Benchmarks for the parallel scalability of our implementation are also available in the Results Section of Chapters 3 and 5.

Chapter 3

Propagation of Stationary States

In this chapter, we evaluate the performance of our implementation of real-time TDDFT with an exactly solvable problem - the time propagation of stationary KS wavefunctions. In spite of the apparent simplicity of this problem, it provides invaluable information concerning not only the numerical stability and accuracy of our code, but its efficiency and scalability as well. We begin by giving the details of the precise tests being performed, and proceed to discuss the actual time integrator used to propagate the stationary KS solution. The chapter concludes with a broad array of results that characterize the performance of our implementation.

Problem Statement

We consider the TDKS equations in the immobile ion limit with initial conditions drawn from a Mermin DFT calculation:

$$i\mathcal{S}\frac{\partial}{\partial t}|\tilde{\psi}_n(t)\rangle = \tilde{\mathcal{H}}_{KS}|\tilde{\psi}_n(t)\rangle \tag{3.1a}$$

$$|\tilde{\psi}_n(t=0)\rangle = |\tilde{\psi}_n^0\rangle, \text{ where } \tilde{\mathcal{H}}_{KS}|\tilde{\psi}_n^0\rangle = \epsilon_n\mathcal{S}|\tilde{\psi}_n^0\rangle \tag{3.1b}$$

Electron temperature has been included in the KS orbitals weights, f_n, that are used to build the density and kinetic energy. To this end, our initial density is given as:

$$n(\mathbf{r}, t=0) = \sum_n f_n|\tilde{\psi}_n^0(\mathbf{r})|^2 \tag{3.2}$$

Here, $f_n \in [0,1]$ are the KS orbital occupancies drawn from a Fermi-Dirac distribution. In the absence of any TD perturbations in $\tilde{\mathcal{H}}_{KS}$ or any mechanism through which the orbital occupancies are modified, the system will remain in the stationary state defined by the initial DFT calculation, and the solution of the above problem analytically is trivial:

$$|\tilde{\psi}_n(t)\rangle = e^{-i\epsilon_n t}|\tilde{\psi}_n^0\rangle \tag{3.3}$$

We will use this analytic solution to verify and benchmark our real-time TDDFT implementation before attempting to do any production science.

Given the disarmingly simple nature of this test case, it is important to consider the difficulties that can arise when solving the TDKS equations. So long as the KS orbitals follow the exact evolution prescribed by Equation 3.3, the KS density will be constant and the KS potential will remain unchanged. In practice, however, at each time step the TDKS orbitals will be updated and integration error may cause the density and potential to deviate from a constant. As the machinery for constructing the density and potential from the updated KS orbitals is quite involved, there is room for additional error to creep in through these processes, as well. First and foremost, this test serves as a simple means of establishing the stability of our implementation against these types of errors.

Beyond issues concerning verification of our implementation, it is interesting to comment on the occupancies (f_n) in Equation 3.2. Numerically these quantities are held fixed to their initial values throughout the entire calculation, and this will be the case for all calculations in subsequent chapters of this report. Coupled with the unitary evolution of the KS orbitals, this guarantees that the sum rule relating the charge density to the number of electrons is satisfied at each time step. It will be of interest in future extensions of our framework to explore models in which the occupancies are allowed to change as a function of time, particularly as a mechanism for non-adiabatic electron-ion coupling.

Results

In all subsequent results, the initial states were achieved from a conventional DFT calculation converged to 10^{-8} eV in the self-consistency cycle of the total energy. In practice, we have found that the convergence of the initial state gives some limit on the energy conservation that can be reasonably expected in the subsequent time evolution. In other words, if we want to conserve energy within 10^{-3} eV, the initial state must be converged to at least that accuracy. Further, all results are achieved using the standard Crank-Nicolson time integrator. For stationary states, there is little benefit to using the predictor-corrector framework, and any timing results can be extrapolated by approximately doubling them.

Accuracy Benchmarks

In the first result, we demonstrate that our implementation accurately reproduces the time evolution described in Equation 3.3. The system under consideration consists of 16 Be atoms each with 2 valence electrons, and integrated with a time step of 2.5 as and using a plane wave cutoff of 300 eV. The initial condition is taken to be the Mermin state at 5000K, requiring 40 KS orbitals. In Figure 3.1, we illustrate the error in representative coefficients of the slowest and fastest KS orbitals relative to their analytic evolution. We note that the global error grows in time, and that this essentially amounts to a phase error. In other words, the amplitude of the orbital oscillation is constant thanks to the unitarity of the integrator, so the error comes about as a spurious accumulation of phase. We anticipate that this accumulation of global error will be largely irrelevant in practice, as the phase of

the KS orbitals is less important in adiabatic TDDFT than the density, which experiences no such growth in error. It is possible, however, that there may be some quantities of interest in TDDFT that are sensitive to phase information, and for these quantities this accumulation of error is controllable by decreasing the time step.

Our next result substantiates our claim that the accumulation of phase error over long times is irrelevant to quantities derived from the density, namely the Hartree energy - a simple physically relevant quantity that is known exactly as a density functional. We consider this contribution to the system's energy rather than the total energy because of difficulties in rigorously defining the latter in TDDFT. In Figure 3.2, we have computed the time-dependent Hartree energy of the system described above. For the purposes of the eventual application to electron-ion dynamics, in which the system must be evolved for 100s-1000s of femtoseconds, using a time step on the scale of attoseconds, it is important to guarantee that the long time stability of TDDFT quantities is achievable within our implementation. To this end, we see that the Hartree energy varies at the level of μeV in the stationary state propagation, even for an initial state drawn from a high temperature Mermin DFT calculation.

It is important to emphasize that even though the stationary state problem is analytically trivial, the numerical method that we have used to arrive at these results is not. Here, we have re-computed the KS Hamiltonian and all associated operators at each time step from the numerically integrated orbitals, so these results confirm that there is not some hidden accumulation of error in the construction of the various potentials and densities of relevance that destabilizes our integrator.

Solver Benchmarks

In Figure 3.3, we consider the computational time required per time step in our CGS solver, as a function of the accuracy desired. Desired accuracy is given in terms of the number of digits to which the CGS residual is zero with respect to the L^2 norm. These results are drawn from a calculation on the same Be system considered above, but with a 400 eV cutoff and 96 KS orbitals. The average time per step for the entire time integration was recorded, with error bars indicating that there is a very small variation in this quantity from step to step. In so far as the time per step scales directly with the number of iterations in the CGS algorithm, this gives some indication of how well conditioned the Crank-Nicolson system is. Here, it is evident that machine precision can be achieved if desired, and that the rate of convergence is empirically observed to be exponential.

To give some indication of how these results scale with the size of the plane wave basis, the scaling of the number of iterations per CGS solve at a fixed accuracy with the plane wave cutoff is presented in Figure 3.4. For these results, we consider calculations with increasingly larger number of KS orbitals as well, to include the effects of solving update equations for higher orbitals in our statistics. These results give us some empirical confidence that increasing the size of our basis set will not have a pathologically adverse effect on the

conditioning of the Crank-Nicolson update equations.

Scalability Benchmarks

In Figure 3.5, strong scaling is illustrated for a WDM system consisting of 30 Xe atoms each with 8 valence electrons, a cutoff of 750 eV and 1024 orbitals at a single k-point, integrated with a time step of 2 as and an accuracy of 8 digits in the CGS solver. The initial condition is taken from the Mermin ground state at 20000K. By strong scaling, we mean that the problem remains fixed while the number of cores on which it is solved is increased. Here, the time per step is recorded and the type of parallelism is constrained to be over orbitals only. We find that there is only negligible deviation from ideal scaling up to 512 cores, illustrating that our implementation can take good advantage of high performance computing resources.

Having achieved good scaling only taking advantage of parallelism over orbitals, it is interesting to see if a further improvement in performance can be achieved by exploiting hybrid parallelism over both plane wave coefficients and orbitals. In Figure 3.6, we vary the number of orbitals per core from 2 (no parallelism over plane waves) to 128, and record the time per step decomposed into contributions from the various underlying stages. From this decomposition, we learn that the dominant cost per time step is the solution of the Crank-Nicolson update equations. Among the other stages of the calculation, there is little variation in the time required with the distribution of work. The evaluation of the PAW operators (augmentation charges and single-center terms) and the calculation of the local potential are essentially insensitive to the work distribution, with the calculation of the charge density showing some weak dependence that is most pronounced for 8 orbitals per core. Beyond the details of the decomposition, it is also evident that the time per step can be reduced significantly by taking advantage of parallelism over orbitals and plane wave coefficients. In the best cases for 16 and 32 orbitals per core, there is a 3-fold reduction in the time per step relative to using parallelism over orbitals alone. One final remark concerning this data is that it highlights that the problem is 'more parallel' with respect to bands than plane wave coefficients. In moving to parallelism over plane wave coefficients alone, performance degrades much more significantly, and even for 128 orbitals per core (far from the pure coefficient parallelism, i.e., 1024), the timing is more than 10x that of the optimal distribution.

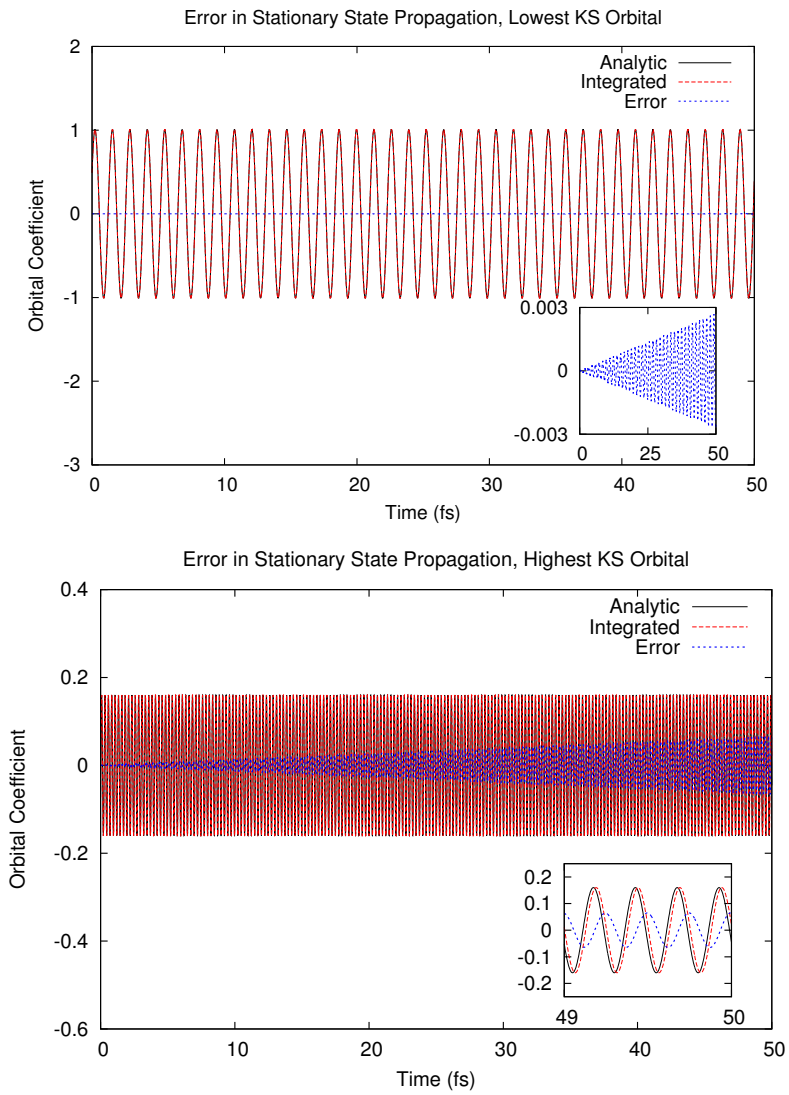

Figure 3.1. Error in the lowest (top) and highest (bottom) TDKS orbitals as a function of time. Insets: Zooming in on linear growth in global error (top) and illustration of accumulated phase error (bottom). System: 16 Be atoms at 5000K.

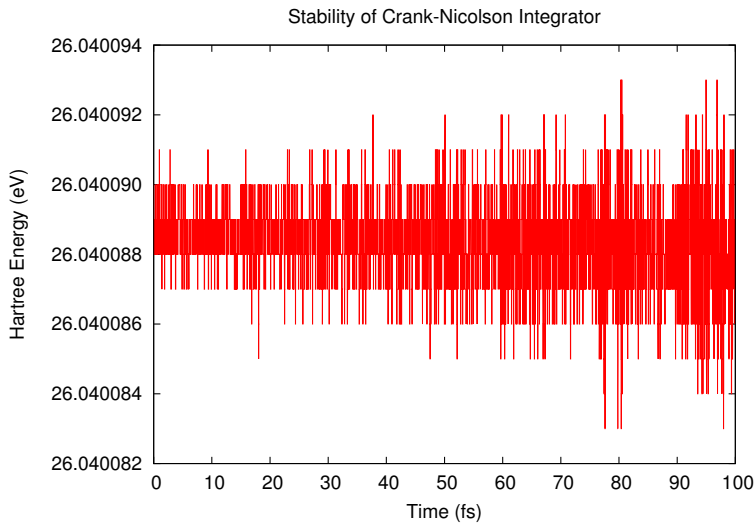

Figure 3.2. Stability of the Hartree energy over thousands of steps for 16 Be atoms initialized at $t = 0$ in the Mermin ground state at 5000K.

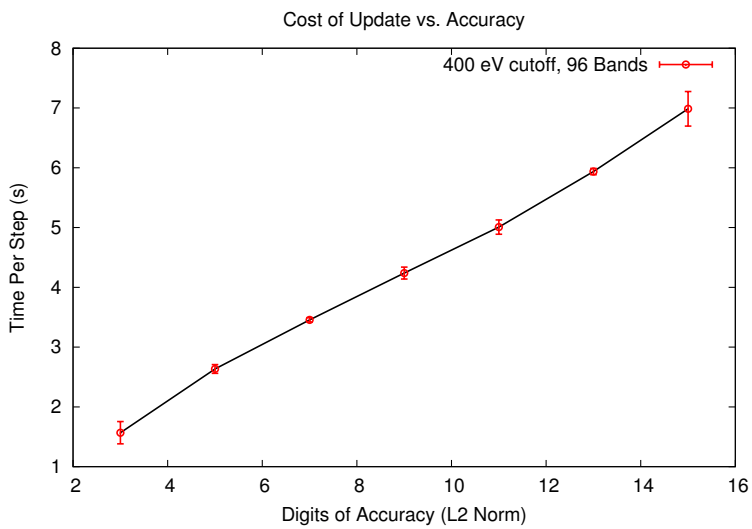

Figure 3.3. Scaling of the time per step with the accuracy guaranteed by the iterative solve. System: 16 Be atoms at 5000K.

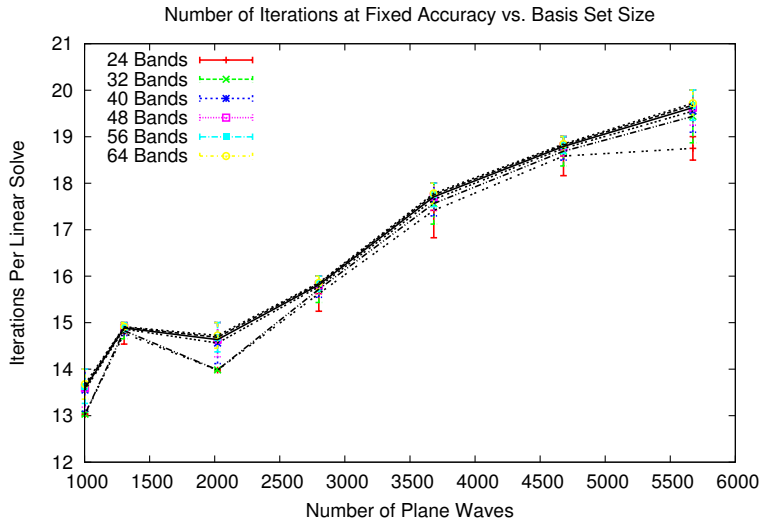

Figure 3.4. Scaling of the number of iterations required to achieve fixed accuracy as a function of the basis set size. System: 16 Be atoms at 5000K.

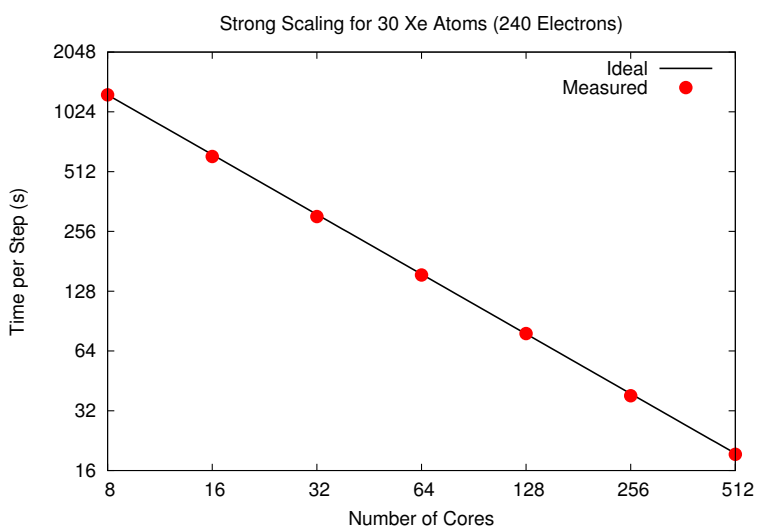

Figure 3.5. Strong scaling of the time per step for a WDM system with 30 Xe atoms and 1024 orbitals.

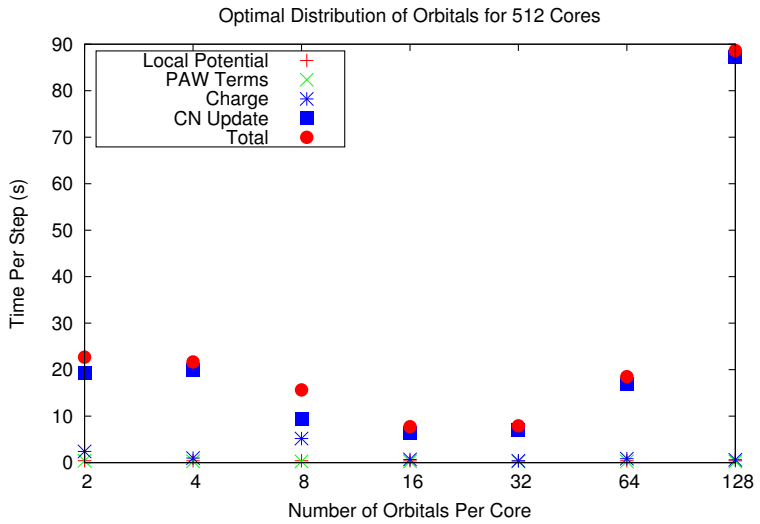

Figure 3.6. The variation in the time per step in changing the number of orbitals per core for 512 cores with 1024 orbitals in total. The time per step is broken into different stages to highlight the dominant cost being the Crank-Nicolson update.

Chapter 4

Calculation of Optical Response

In this chapter, the application of our real-time TDDFT implementation to the calculation of optical response is presented. We begin by considering an approach developed by Yabana and Bertsch [35], for finite systems, in which the ground state KS wavefunction is perturbed, and the subsequent evolution of the system's dipole moment is related to its dipole optical response. We begin by providing a brief overview of the underlying theory, details germane to its implementation, and results that demonstrate agreement with established data from the literature. It is pertinent to note that while we are computing the response of finite systems, in practice the calculation is done within a periodic supercell which is large enough that there is negligible charge density near the boundary of the computational domain. While there will remain a spurious interaction between images, the leading order contribution will be due to a dipole-dipole interaction that dies off rapidly with supercell size. Details pertinent to ongoing efforts in extending these methods to optical response in extended systems are given in Appendix A.2. These tests are important because they show that we can capture dynamics beyond the stationary state.

Problem Statement

We consider the evolution of the KS state under the action of Equation 2.4 in the limit of immobile ions, and adding an external perturbing electric field, $\mathbf{E}(t)$, to the KS Hamiltonian. The field is spatially homogeneous and is applied instantaneously. It is given as:

$$\mathbf{E}(t) = \mathbf{A}_0 \delta(t) \tag{4.1}$$

For $t < 0$ the system will be described by a set of orbitals with occupations, f_n, set within the Mermin DFT formalism such that $0 \leq f_n \leq 1$. The effect of the perturbing field will be to phase shift each orbital while leaving its occupation invariant. This scenario is mathematically codified below, with Equation 4.2a describing the initial conditions for 2.4 in terms of the unperturbed orbitals described by Equation 4.2b:

$$\mathcal{T}|\tilde{\psi}_n(t = 0^+)\rangle = e^{i\mathbf{A}_0 \cdot \hat{\mathbf{r}}} \mathcal{T}|\tilde{\psi}_n^0\rangle \tag{4.2a}$$

$$\tilde{\mathcal{H}}_{KS}\,[t < 0]\,|\tilde{\psi}_n^0\rangle = \epsilon_n \mathcal{S}|\tilde{\psi}_n^0\rangle \tag{4.2b}$$

As the field acts instantaneously at $t = 0$, and it leaves the density (and equivalently, the KS potential) invariant, it is of interest to consider what will cause nontrivial dynamics for $t > 0$. Simply put, it is the jump in the KS kinetic energy at $t = 0$, induced by the position-dependent phase-shift applied to the stationary orbitals. Formally, this causes no problems within the TDDFT framework, as the TDDFT potential is uniquely determined by not only the density, but the initial state of the system. For weak fields, this jump in the initial kinetic energy of the system manifests in terms of a redistribution of the KS configurations from the $t < 0$ stationary determinant to a linear combination of this and dipole-excited configurations. The subsequent time evolution of the density will allow us to compute the relative intensities and energies associated with transitions between these configurations.

With the goal of extracting this information in mind, we consider the analytic evolution of the system for small $\mathbf{A}_0$. We start by writing down the single Slater determinant AE many-body wavefunction, $|\Psi(t)\rangle$, immediately following the perturbation:

$$|\Psi(t = 0^+)\rangle \approx \left(1 + i\mathbf{A}_0 \cdot \sum_j \hat{\mathbf{r}}_j\right) |\Psi(t = 0^-)\rangle + \mathcal{O}(|\mathbf{A}_0|^2) \tag{4.3}$$

Here we have Taylor expanded the exponential resulting from the impulsive action of the field, and the sum on j is over all electrons. We can easily recognize that this is the system's dipole operator:

$$|\Psi(t = 0^+)\rangle \approx (1 + i\mathbf{A}_0 \cdot \hat{\boldsymbol{\mu}}) |\Psi(t = 0^-)\rangle + \mathcal{O}(|\mathbf{A}_0|^2) \tag{4.4}$$

We can now see what was stated in the previous paragraph - that the $t = 0^+$ state becomes a linear combination of the initial many-body determinant and dipole-allowed excitations from that state. Labeling the $t < 0$ many-body state $|g\rangle$, and these excitations $|e\rangle$, the dynamics for $t > 0$ can be written as:

$$|\Psi(t)\rangle = c_g|g\rangle + \sum_e c_e e^{-i\epsilon_e t}|e\rangle \tag{4.5a}$$

$$c_g = 1 + i\mathbf{A}_0 \cdot \langle g|\boldsymbol{\mu}|g\rangle \tag{4.5b}$$

$$c_e = i\mathbf{A}_0 \cdot \langle e|\boldsymbol{\mu}|g\rangle \tag{4.5c}$$

Here, ϵ_e are the unknown transition energies, and the coefficients are related to the intensity of the associated transitions. However, as we are working within the framework of DFT and we have no direct knowledge of the excited configurations, we need to find a way to get these quantities from the TD density. Retaining only terms that are linear in $\mathbf{A}_0$, the TD density given by the TDKS state in Equation 4.5a is written as:

$$n(\mathbf{r}, t) = n_0(\mathbf{r}) + \sum_e \left(c_e e^{-i\epsilon_e t}\langle g|\hat{n}(\mathbf{r})|e\rangle + \text{ c.c.}\right) + \mathcal{O}(|\mathbf{A}_0|^2) \tag{4.6}$$

From which it is clear that we can write the TD dipole moment as:

$$\boldsymbol{\mu}(t) = \int d\mathbf{r}\; n(\mathbf{r}, t)\; \mathbf{r} \tag{4.7a}$$

$$\boldsymbol{\mu}(t) = \boldsymbol{\mu}(0) - 2\mathbf{A}_0 \cdot \langle e|\boldsymbol{\mu}|g\rangle \sin(\epsilon_e t)\langle g|\boldsymbol{\mu}|e\rangle + \mathcal{O}(|\mathbf{A}_0|^2) \tag{4.7b}$$

Given this form of the TD dipole moment we can extract the locations of dipole-transitions and their associated strengths.

In practice, the TDKS equations are solved subject to the initial conditions in Equation 4.2a, and the TD dipole moment is computed at each time step for T_{sim} units of time. Fitting to the form given in Equation 4.7b is then easiest in the energy domain, wherein the following relationship holds:

$$\overline{\overline{\mathbf{S}}}(\epsilon) \cdot \mathbf{u}_{\mathbf{A}_0} \sim \lim_{\mathbf{A}_0 \to 0} \frac{1}{|\mathbf{A}_0|} \int_0^{T_{sim}} dt \sin(\epsilon t) w(t) \left(\boldsymbol{\mu}(t) - \boldsymbol{\mu}(0)\right) \tag{4.8}$$

Here, $\overline{\overline{\mathbf{S}}}(\epsilon)$ is the dipole polarizability tensor associated with the system, $\mathbf{u}_{\mathbf{A}_0}$ is a unit vector along $\mathbf{A}_0$, and $w(t)$ is some windowing function that renders the integrand 0 for $t \geq T_{sim}$. The windowing function is necessary to facilitate spectral analysis of the necessarily time-limited sampled data. A convenient choice is a Gaussian window, $w(t) = \exp(-\gamma t^2)$, where $\gamma = (\hbar/E_b)^2$ and E_b can be interpreted as an artificial broadening energy.

Results

We present the optical response of two small molecules that have been previously characterized in the literature using this same technique. This set of tests has been previously applied to a plane wave pseudopotential implementation of TDDFT [31], as well as real-space implementations [36, 37]. In all cases where it is applicable, the parameters from [31] have been utilized, given the similarities between ultrasoft pseudopotentials and PAWs.

The first molecule under consideration is a sodium dimer, with bond length 3.00$\mathring{A}$. Its dipole response averaged over perturbing fields along the dimer axis and two orthogonal vectors transverse to the axis will give the response that would be observed in a gas-phase experiment. These results are given in Figure 4.1. Using the same setup as earlier calculations [31], the dimer was placed at the center of a 12.00$\mathring{A}$ $\times$ 10.00$\mathring{A}$ $\times$ 10.00$\mathring{A}$ box, and a plane wave cutoff of 300 eV was used for the basis set. The time step was chosen to be 2 as, the system was perturbed by a field of magnitude 0.01$\mathring{A}^{-1}$, and evolved for 20 fs in each numerical experiment. Given $\boldsymbol{\mu}(t)$ for each orientation of the perturbing field, Equation 4.8 is evaluated using a Gaussian window with a width of approximately 0.1 eV. Comparing to spectra available in [36, 31], these results are in good agreement with other numerical calculations, as well as experimental spectra. It is worth noting for later comparison, that the peak just above 2 eV is only excited by a field perturbing along the dimer axis, whereas the peak just below 3 eV is only excited by fields perturbing transverse to it. The weak feature around 4 eV is excited by all 3 perturbing fields, though there is a small shift in energy between the transverse and longitudinal perturbation.

The next molecule under consideration is benzene, with C-C bond length of 1.39$\mathring{A}$, and C-H bond length of 1.10$\mathring{A}$. Again, the dipole response is averaged over three orthogonal

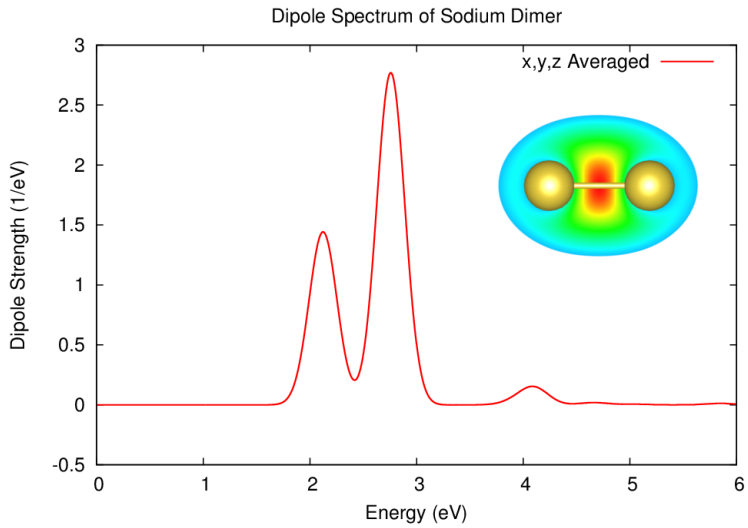

Figure 4.1. Dipole absorption spectrum of a sodium dimer. Inset: molecular structure and the ground state charge density.

perturbing fields to give the gas-phase spectra. Results are given in Figure 4.2. The molecule was placed at the center of a $12.94\mathring{A} \times 10.00\mathring{A} \times 7.00\mathring{A}$ box, with the plane of the molecule orthogonal to the short axis, and a plane wave cutoff of 250 eV. A time step of 2.5 as was set, the perturbing field strength was set to $0.01\mathring{A}^{-1}$, and the system was evolved for 11.85 fs. A Gaussian window was again used in extracting the spectrum, but with a larger width (approximately 0.25 eV). Again, good agreement is found between numerical results in [37, 31], which compare favorably with experiment.

Our final result is a brief analysis of the optical response of the sodium dimer at finite temperature with fixed nuclei presented in Figure 4.3. Here, we compute the spectrum assuming that the electrons of the cold molecule are instantaneously heated to a nonzero temperature. This is intended to be a crude model of the conditions in a laser shock experiment. In practice, this amounts to generating the initial KS wavefunction in Equation 4.2 from a Mermin DFT calculation carried out at a specified temperature, from a molecular geometry with the ions held at the cold bond length ($3.00\mathring{A}$). We note that while this has been our practice in the previous calculations, the temperatures have been sufficiently low that the orbital occupancies have been indistinguishable from a zero temperature calculation. Results for electron temperatures of 300K, 3000K, 6000K, and 10000K are presented in 4.3. Here the same geometry, cutoff, and time integration have been used as in the previous sodium dimer result. It is worth noting that the number of bands is increased at high temperature (from 4 at 300 K to 13 at 10000 K) to accommodate the occupation of high-lying KS orbitals. In these results we have only computed the spectrum for a perturbing field along the dimer axis, to highlight the effect that nonzero temperatures have on the optical spectrum. The 300 K spectrum retains the same structure that it had in Figure 4.1, with the feature just

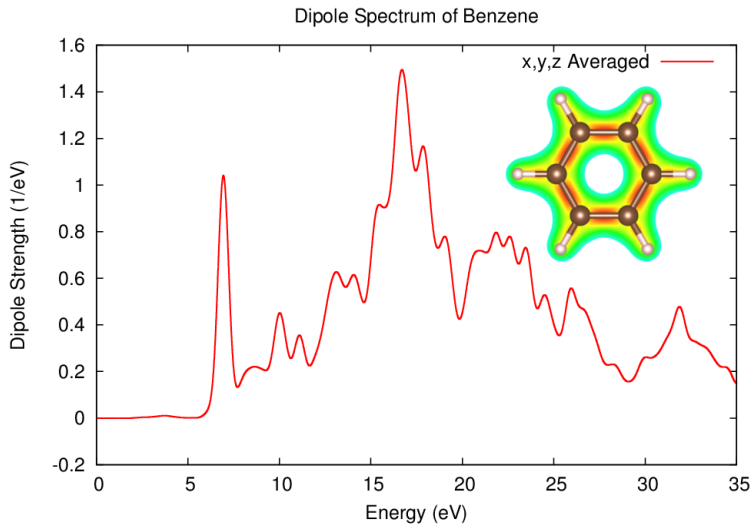

Figure 4.2. Dipole absorption spectrum of benzene. Inset: molecular structure and the ground state charge density.

above 2 eV only being visible due to our restriction of the polarization. As the electronic temperature is elevated, new peaks appear in the dipole spectrum as transitions out of both higher and lower orbitals are now possible.

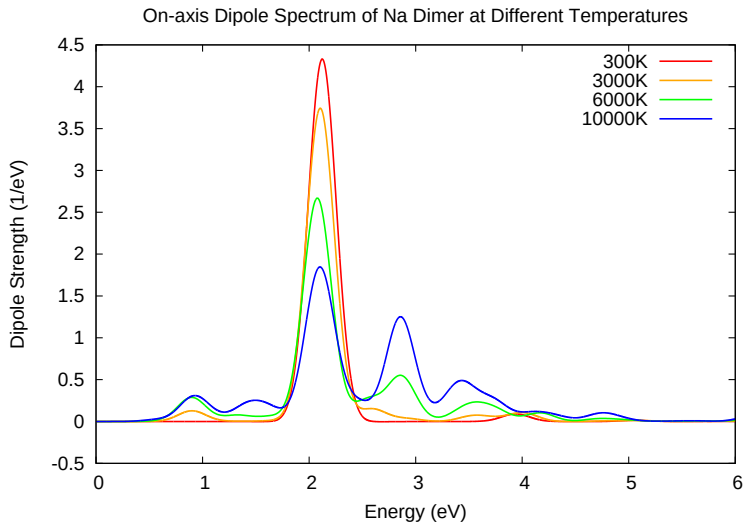

Figure 4.3. The dipole absorption spectrum of a sodium dimer at finite temperature. Initial conditions are drawn from Mermin DFT calculations at the indicated temperatures. Result are only due to a perturbing field applied along the dimer axis.

Chapter 5

Electron-Ion Dynamics and Stopping Power

In this chapter, we relax the previous restriction that the ions remain immobile. To this end Ehrenfest-TDDFT is considered. This is an additional model beyond TDDFT. Two results are demonstrated - one in which a computational advantage of this framework over DFT-MD is made apparent, and another in which Ehrenfest forces are used to compute the stopping power of a proton in a cold solid.

Ehrenfest-TDDFT

In Ehrenfest-TDDFT, ionic forces are computed using the instantaneous real-time electronic state determined by the evolution of the TDKS equations. This stands in contrast to DFT-MD calculations wherein the electrons remain in the ground state computed using conventional DFT, and the ionic forces are determined by these states alone. Consequently, ionic forces in DFT-MD have no knowledge of non-equilibrium electron dynamics. However, the form of the forces in both frameworks is quite similar, and minimal modifications are needed to arrive at reasonable forces given the existing PAW code on which our framework is built.

Within the PAW formalism, the force acting on the Ith ion is given as:

$$\mathbf{F}_I = -\frac{dE_{el}^{PAW}}{d\mathbf{R}_I} = -\frac{\partial E_{el}^{PAW}}{\partial \mathbf{R}_I} + \sum_n f_n \epsilon_n \langle \tilde{\psi}_n | \frac{d\mathcal{S}}{d\mathbf{R}_I} | \tilde{\psi}_n \rangle \tag{5.1}$$

This specific form will work for both DFT-MD and Ehrenfest-TDDFT, with the only significant difference being the electronic state that is being fed into Equation 5.1. In DFT-MD, $|\tilde{\psi}_n\rangle$ is determined from the solution of Equation 2.3 for a given set of ionic positions. In Ehrenfest-TDDFT, $|\tilde{\psi}_n\rangle$ is computed from the solution of Equation 2.5.

While this similarity is convenient for preliminary verification it is useful to note that the authors of [38] have indicated that these are not the proper energy conserving forces for Ehrenfest-TDDFT. Instead, these are referred to as 'incomplete basis set corrected' (IBSC) forces, which provide reasonable energy conservation only for short periods of time (< 10

fs). The more rigorous 'energy conserving' (EC) forces discussed in [38] can be rewritten as a correction to the IBSC forces as follows:

$$\mathbf{F}_I^{EC} = \mathbf{F}_I + \sum_n f_n \langle \tilde{\psi}_n | \frac{d\mathcal{T}^\dagger}{d\mathbf{R}_I} \mathcal{T}\mathcal{S}^{-1}\tilde{\mathcal{H}}_{KS} + h.c. - \epsilon_n \frac{d\mathcal{S}}{d\mathbf{R}_I} | \tilde{\psi}_n \rangle \tag{5.2}$$

However, as the results in this chapter are taken over short times they are somewhat insensitive to this correction, so the following results are computed using forces computed within Equation 5.1.

The first result in this chapter illustrates an advantageous feature of Ehrenfest-TDDFT over DFT-MD. As the electronic state in Ehrenfest-TDDFT is determined via the numerical integration of the TDKS equations, rather than a full self-consistent conventional DFT calculation, the computational cost of the two schemes is quite different. In particular, Figure 5.1 demonstrates that the parallel scalability of Ehrenfest-TDDFT is superior to DFT-MD. Here, the same system as used in the scalability results in Figure 3.5 is utilized (30 Xe atoms, 240 electrons). The parallel speed up associated with the time per step of Ehrenfest-TDDFT and DFT-MD is compared for equal time steps and accuracy (2 as and 8 digits). As is evident, near-perfect scaling is achieved using Ehrenfest-TDDFT up to 512 cores, while it saturates beyond 32 cores using DFT-MD. This is essentially a factor of the orthogonalization required at each step in a DFT-MD calculation. As different parallelization strategies are optimal for applying the KS Hamiltonian and orthogonalization, the implementation that we use employs data redistribution to balance the respective bottlenecks of both. As we only require a parallelization strategy for applying the KS Hamiltonian (by way of solving the Crank-Nicolson update equations), we escape having to perform this redistribution. This performance is independent of whether or not the predictor-corrector version of the Crank-Nicolson integrator is applied.

While the crossover in speed up occurs at 32 cores, it is worth noting that the crossover in actual time per step occurs at 128 cores. On 8 cores, the DFT-MD time step is actually 2.9 times faster in terms of time per step. It is worth noting that comparing these times is somewhat limited practically, as DFT-MD can employ a much longer time step than Ehrenfest-TDDFT (100s of as instead of 1s of as). However, this is still artificially favorable to DFT-MD because the electronic state changes very little between steps. This represents a best case scenario with a very good initial guess for the SCF cycle in the conventional DFT calculation, and a more realistic DFT-MD step will typically require more iterations to achieve self-consistency.

Stopping Power

In the following, we consider the calculation of stopping power using Ehrenfest-TDDFT forces. These calculations proceed as follows:

- An initial state is prepared in which the electronic ground state of some projectile ion embedded in a crystalline supercell is computed.

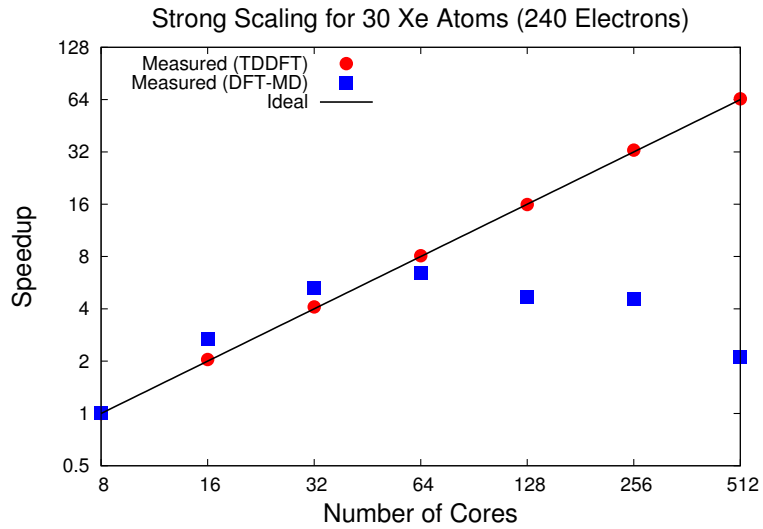

Figure 5.1. Scalability comparison of DFT-MD and Ehrenfest-TDDFT. Both methods are evaluated using the same time step, presenting a simplest-case scenario for DFT-MD.

- An Ehrenfest-TDDFT calculation is evolved from this state, in which the projectile ion is dragged through the supercell at a fixed velocity.
- Forces acting on the projectile ion are evaluated at each time step, permitting the calculation of the work done by the system on the projectile.

This procedure is validated using results from [39], wherein Ehrenfest-TDDFT calculations of the stopping power of a proton in Al within the SIESTA code were compared to the SRIM/TRIM database [40].

Here, we considered a supercell of 64 Al atoms on a face-centered cubic lattice with lattice constant 4.05$\mathring{A}$. The projectile H atom was set along a trajectory along the $\langle 100 \rangle$ direction. The initial state was computed at a 500 eV cutoff on a 2×4×4 mesh of k-points in the first Brillouin Zone using the local density approximation (LDA) to the exchange-correlation functional. This same cutoff and set of k-points were used in the Ehrenfest-TDDFT calculation, as well as an adiabatic LDA functional. As in [39], both channeling and off-channeling trajectories are considered, with geometries illustrated in Figure 5.2. Further, calculations were performed in which both the non-projectile ions were kept fixed, and allowed to move subject to Ehrenfest forces. No significant difference was found between these two scenarios, and data from the former are presented. This is due to the high velocity of the projectile ion, wherein 1-10 fs is required for the traversal of the unit cell. While the ion can significantly redistribute the very light electrons in this short period of time, it cannot similarly affect the much heavier ions.

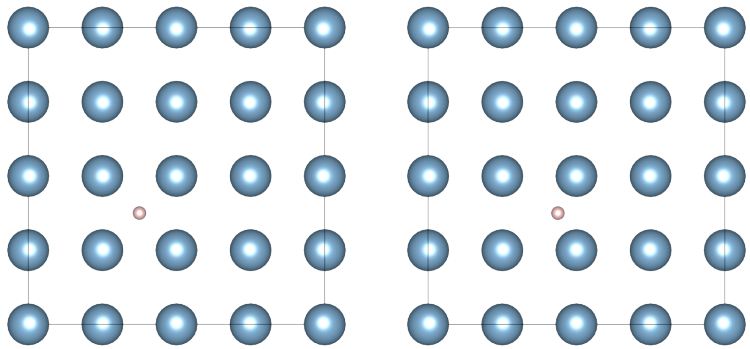

Figure 5.2. View along the ⟨100⟩ direction for channeling (left) and off-channeling (right) trajectories. Blue spheres represent Al atoms, while the pink sphere indicates the proton.

The results of our calculations are presented in Figure 5.3. A trend similar to that observed in [39] is evident, wherein the stopping power is reproduced well below the peak velocity (1.5 a.u.), but is underestimated above this velocity. These previous authors indicate that this may be a deficiency of their pseudopotential - in other words, they are missing core excitations brought about by only having 3 valence electrons. Preliminary results comparing both 3 and 11 electron PAWs for Al indicate that this is likely not the case, and the results are essentially insensitive to the number of valence electrons. We postulate that this discrepancy may then be due to missing non-adiabatic effects and/or finite size effects.

Still, there is some discrepancy between our result and [39] as the authors predict significantly different stopping powers for channeling and off-channeling trajectories. While this is not observed in our calculations our result is consistent with our physical intuition. As Al is a good metal, we expect the electronic charge density to be relatively uniform throughout. Only off-channeling trajectories that pass very close to knock-on will give significantly different results for stopping power. Directly investigating the charge density seen by the channeling and off-channeling protons, we find a negligible difference between the two trajectories. Because the charge densities are nearly the same, and we are using an adiabatic local exchange-correlation functional, the electronic contribution to the stopping is virtually identical for the two trajectories. The only remaining discrepancy between the trajectories is due to the ionic contribution to the stopping, which should be small at these velocities. In Figure 5.4, the stopping force acting on the proton in exemplary channeling and off-channeling trajectories at the same velocity are compared. While the off-channeling proton experiences a more dramatic variation in the force that it experiences, the average force is nearly the same as for a channeling proton.

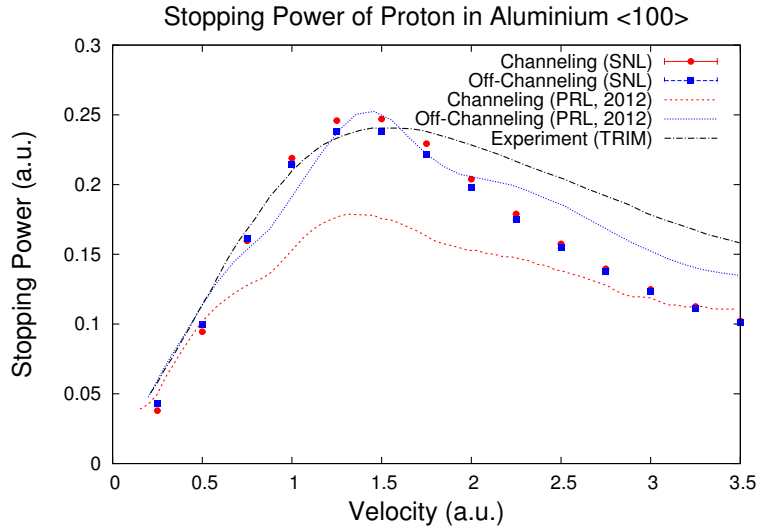

Figure 5.3. Stopping power of a proton in cold Al compared to SRIM/TRIM database and results published in [39]. Channeling $\langle 100 \rangle$ and off-channeling trajectories give similar results.

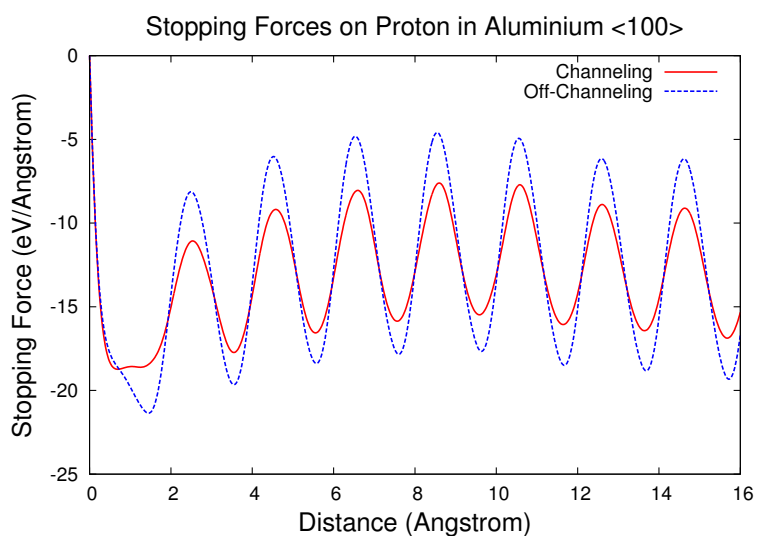

Figure 5.4. Force acting on proton in the stopping power calculations for channeling and off-channeling trajectories.

Chapter 6

Conclusion

Summary

In this report, progress towards a capability for first principles calculations of warm dense systems using Ehrenfest-TDDFT was presented. Our results indicate that our implementation is numerically sound in terms of accuracy, efficiency, and scalability. Further we have reproduced results from the literature concerning optical response and stopping power, indicating that our implementation is currently on track to producing novel production scientific results. In what follows, we will outline progress to be made in the coming months.

Future Work

The calculation of optical response in bulk WDM systems is of primary interest. In contrast to the ordered systems studied in [41], the response of WDM will require averaging over the results of many calculations started from independent ionic configurations drawn from either DFT-MD or Ehrenfest-TDDFT at the appropriate temperature. Even so, we anticipate improvements relative to the state-of-the-art Kubo-Greenwood calculations which are based upon linear response theory. These calculations rely upon the DFT-MD framework and require a number of virtual states that scales directly with temperature to achieve convergence. To this end, the orthogonalization bottleneck discussed briefly in Chapter 5 becomes increasingly restrictive at higher temperatures. Investigations are currently under way to place bounds on the parameter space over which optical response calculations using TDDFT become favorable relative to the Kubo-Greenwood framework. Even beyond improving upon Kubo-Greenwood calculations, we will pursue collaborations with other DFT-MD capabilities at Sandia to find other applications facilitated by this new capability. We anticipate that our framework will be useful to applications ranging from surface science and soft matter physics, to battery technology and quantum information.

The next item of interest is the calculation of the XRTS DSF discussed in Chapter 1 for a number of relevant systems, such as Be. Here, we are interested in the direct evaluation of Equation 1.3 within Ehrenfest-TDDFT. This is a relatively straightforward task, though there are a number of practical issues for which intuition will have to be developed. Among

them are the manner in which the ensemble average in Equation 1.3 is taken and details concerning the importance of using the AE charge relative to the PS charge. Questions concerning ensemble averaging have led us to deeper problems within the TDDFT formalism, particularly what it means to be doing TDDFT in the canonical ensemble. At present, we capture thermal effects by propagating from a Mermin density, which is representative of the density of the thermal equilibrium state. Throughout the time evolution of this density, the KS orbital occupancies are fixed to those of the initial Mermin state. At this point, it is not clear how good of an approximation this is. In so far as the adiabatic local/semilocal functionals that we are currently employing have no means of distinguishing between an ensemble averaged density from the canonical ensemble, and a density from the microcanonical ensemble, there is no doubt some new form of 'self-interaction error' introduced. We are looking to the base of knowledge being developed germane to finite temperature functionals for some means of quantifying how this type of error scales with temperature.

These questions lead naturally to the final issue that we seek to address, and that is improvements of the electron-ion dynamics beyond Ehrenfest-TDDFT. We are particularly interested in capturing non-adiabatic effects necessary to electron-ion thermalization. To this end, we are investigating frameworks wherein the KS orbital occupancies are no longer constrained to remain fixed throughout the time evolution. The Landau-Zener formalism currently seems like the most promising avenue, wherein we have a continuous time model from which we will develop an equation of motion for the orbital occupancies. Consistent with changes in the occupancies, non-adiabatic forces will be applied to the ions, allowing for the electron subsystem to confer some of its energy directly to the ionic subsystem. One can then imagine calculations in which, starting from a strongly non-equilibrium electronic state, the rate at which the electrons and ions equilibrate with themselves and each other are accessible. These types of calculations have tremendous importance to informing higher level models used in developing ICF technology.

References

[1] Seth Root, Kyle R Cochrane, John H Carpenter, and Thomas R Mattsson. Carbon dioxide shock and reshock equation of state data to 8 Mbar: Experiments and simulations. *Physical Review A*, 87(22):224102, June 2013.

[2] Seth Root, Rudolph J Magyar, John H Carpenter, David L Hanson, and Thomas R Mattsson. Shock Compression of a Fifth Period Element: Liquid Xenon to 840 GPa. *Physical Review Letters*, 105(8):085501, August 2010.

[3] M D Knudson, M P Desjarlais, and D H Dolan. Shock-Wave Exploration of the High-Pressure Phases of Carbon. *Science*, 322(5909):1822–1825, December 2008.

[4] Michael P Desjarlais. Density-functional calculations of the liquid deuterium Hugoniot, reshock, and reverberation timing. *Physical Review A*, 68(6):064204, August 2003.

[5] M D Knudson, D L Hanson, J E Bailey, C A Hall, and J R Asay. Equation of State Measurements in Liquid Deuterium to 70 GPa. *Physical Review Letters*, 87(22):225501, November 2001.

[6] Nadine Nettelmann, Bastian Holst, André Kietzmann, Martin French, Ronald Redmer, and David Blaschke. Ab Initio Equation of State Data for Hydrogen, Helium, and Water and the Internal Structure of Jupiter. *The Astrophysical Journal*, 683(2):1217–1228, August 2008.

[7] Bastian Holst and Ronald Redmer. Thermophysical properties of warm dense hydrogen using quantum molecular dynamics simulations. *Physical Review A*, 77(18):184201, May 2008.

[8] Siegfried H Glenzer and R Redmer. X-ray Thomson scattering in high energy density plasmas. *Reviews of Modern Physics*, 81(4):1625–1663, December 2009.

[9] K-U Plagemann, P Sperling, R Thiele, M P Desjarlais, C Fortmann, T Döppner, H J Lee, Siegfried H Glenzer, and R Redmer. Dynamic structure factor in warm dense beryllium. *New Journal of Physics*, 14(5):055020, May 2012.

[10] R Thiele, T Bornath, C Fortmann, A Höll, R Redmer, H Reinholz, G Röpke, A Wierling, S Glenzer, and G Gregori. Plasmon resonance in warm dense matter. *Physical Review E*, 78(2):026411, August 2008.

[11] T Döppner, P F Davis, A L Kritcher, O L Landen, H J Lee, S P Regan, and S H Glenzer. Using collective x-ray Thomson scattering to measure temperature and density of warm dense matter. In James Dunn and Gregory J Tallents, editors, *SPIE Optical Engineering + Applications*, pages 74510H–74510H–9. International Society for Optics and Photonics, August 2009.

[12] G Gregori, Siegfried H Glenzer, W Rozmus, R W Lee, and O L Landen. Theoretical model of x-ray scattering as a dense matter probe. *Physical Review E*, 67(2):026412, February 2003.

[13] C Fortmann, T Bornath, R Redmer, H Reinholz, G Röpke, V Schwarz, and R Thiele. X-ray Thomson scattering cross-section in strongly correlated plasmas. *Laser and Particle Beams*, 27(02):311, April 2009.

[14] G Gregori. Generalized x-ray scattering cross section from nonequilibrium plasmas. *Physical Review E*, 74(2):026402, August 2006.

[15] J Chihara. Interaction of photons with plasmas and liquid metals - photoabsorption and scattering - Abstract - Journal of Physics: Condensed Matter - IOPscience. *J. Phys. Condens. Matter*, 12:231, 2000.

[16] Arto Sakko, Angel Rubio, Mikko Hakala, and Keijo Hämäläinen. Time-dependent density functional approach for the calculation of inelastic x-ray scattering spectra of molecules. *Journal of Chemical Physics*, 133(17):174111–174111–6, November 2010.

[17] Erich Runge and E K U Gross. Density-Functional Theory for Time-Dependent Systems. *Physical Review Letters*, 52(12):997–1000, March 1984.

[18] Tie-cheng Li and Pei-qing Tong. Hohenberg-Kohn theorem for time-dependent ensembles. *Physical Review A*, 31(3):1950–1951, March 1985.

[19] Tie-cheng Li and Yanmin Li. Kohn-Sham equation for time-dependent ensembles. *Physical Review A*, 31(6):3970–3971, June 1985.

[20] G Kresse. Efficient iterative schemes for ab initio total-energy calculations using a plane-wave basis set. *Physical Review A*, 54(16):11169–11186, October 1996.

[21] Georg Kresse and Jürgen Furthmüller. Efficiency of ab-initio total energy calculations for metals and semiconductors using a plane-wave basis set. *Computational Materials Science*, 6(1):15–50, 1996.

[22] Georg Kresse and D Joubert. From ultrasoft pseudopotentials to the projector augmented-wave method. *Physical Review B*, 59(3):1758, 1999.

[23] V Nazarov, J Pitarke, Y Takada, G Vignale, and Y C Chang. Including nonlocality in the exchange-correlation kernel from time-dependent current density functional theory: Application to the stopping power of electron liquids. *Physical Review A*, 76(20):205103, November 2007.

[24] Peter E Blöchl. Projector augmented-wave method. *Physical Review B*, 50(24):17953, 1994.

[25] David Vanderbilt. Optimally smooth norm-conserving pseudopotentials. *Physical Review A*, 32(12):8412–8415, December 1985.

[26] Kari Laasonen, Roberto Car, Changyol Lee, and David Vanderbilt. Implementation of ultrasoft pseudopotentials in ab initio molecular dynamics. *Physical Review A*, 43(8):6796–6799, March 1991.

[27] C Lubich. Integrators for Quantum Dynamics: A Numerical Analyst's Brief Review. In J Grotendorst, D Marx, and A Muramatsu, editors, *Quantum Simulations of Complex Many-Body Systems: From Theory to Algorithms*, pages 459–466. John von Neumann Institute for Computing, 2002.

[28] Tobias Jahnke and Christian Lubich. Numerical integrators for quantum dynamics close to the adiabatic limit. *Numerische Mathematik*, 94(2):289–314, April 2003.

[29] Tobias Jahnke. Long-Time-Step Integrators for Almost-Adiabatic Quantum Dynamics. *SIAM Journal on Scientific Computing*, 25(6):2145–2164, January 2004.

[30] Alberto Castro, Miguel A L Marques, and Angel Rubio. Propagators for the time-dependent Kohn–Sham equations. *Journal of Chemical Physics*, 121(8):3425–3433, August 2004.

[31] Xiaofeng Qian, Ju Li, Xi Lin, and Sidney Yip. Time-dependent density functional theory with ultrasoft pseudopotentials: Real-time electron propagation across a molecular junction. *Physical Review A*, 73(3):035408, January 2006.

[32] Tobias Jahnke and C Lubich. Error Bounds for Exponential Operator Splittings. *BIT*, 40(4):735–744, 2000.

[33] André Schleife, Erik W Draeger, Yosuke Kanai, and Alfredo A Correa. Plane-wave pseudopotential implementation of explicit integrators for time-dependent Kohn-Sham equations in large-scale simulations. *Journal of Chemical Physics*, 137:22A546, 2012.

[34] Peter Sonneveld. CGS, A Fast Lanczos-Type Solver for Nonsymmetric Linear systems. *SIAM Journal on Scientific and Statistical Computing*, 10(1):36–52, January 1989.

[35] Kazuhiro Yabana and G F Bertsch. Time-dependent local-density approximation in real time. *Physical Review A*, 54(7):4484–4487, August 1996.

[36] Miguel A L Marques, Alberto Castro, and Angel Rubio. Assessment of exchange-correlation functionals for the calculation of dynamical properties of small clusters in time-dependent density functional theory. *Journal of Chemical Physics*, 115(7):3006–3014, 2001.

[37] Miguel A L Marques. octopus: a first-principles tool for excited electron–ion dynamics. *Computer Physics Communications*, 151(1):60–78, March 2003.

[38] Ari Ojanperä, Ville Havu, Lauri Lehtovaara, and Martti Puska. Nonadiabatic Ehrenfest molecular dynamics within the projector augmented-wave method. *Journal of Chemical Physics*, 136(14):144103–144103–9, 2012.

[39] Alfredo A Correa, Jorge Kohanoff, Emilio Artacho, Daniel Sánchez-Portal, and Alfredo Caro. Nonadiabatic Forces in Ion-Solid Interactions: The Initial Stages of Radiation Damage. *Physical Review Letters*, 108(21):213201, May 2012.

[40] James F Ziegler. SRIM-2003. *Nuclear Instruments and Methods in Physics Research Section B: Beam Interactions with Materials and Atoms*, 219-220:1027–1036, June 2004.

[41] G F Bertsch, J I Iwata, Angel Rubio, and Kazuhiro Yabana. Real-space, real-time method for the dielectric function. *Physical Review A*, 62(12):7998–8002, September 2000.

[42] George B Arfken and Hans J Weber. Mathematical methods for physicists 6th ed. 2005.

Appendix A

A.1 Matrix Elements

In this Section, details are given concerning the evaluation of the operators in the Crank-Nicolson update equations and their modification in the presence of ionic motion. In so far as our implementation makes use of an iterative solution of the associated equations, only the effect of these operators on some PS orbital $|\tilde{\psi}_n\rangle$ need be considered, as the individual matrix elements of the operators are never evaluated and stored.

A.1.1 Crank-Nicolson Update Operator

We begin by considering the steps needed for the solution of Equation 2.7 for every $|\tilde{\psi}_n\rangle$ at each time step. These consist of:

1. Computing the RHS from a matrix-vector product of $\left[\mathcal{S} - \frac{i\Delta t}{2}\tilde{\mathcal{H}}_{KS}(t)\right]$ and $|\tilde{\psi}_n(t)\rangle$.
2. Given the RHS product and some initial guess (typically $|\tilde{\psi}_n(t)\rangle$) solve for $|\tilde{\psi}_n(t+\Delta t)\rangle$ from products of $\left[\mathcal{S} + \frac{i\Delta t}{2}\tilde{\mathcal{H}}_{KS}(t)\right]$ and a sequence of iterate PS kets.

As these two operators differ by a sign in the second term, a single routine for evaluating products with $\left[\mathcal{S} \pm \frac{i\Delta t}{2}\tilde{\mathcal{H}}_{KS}(t)\right]$ was implemented. The evaluation of a matrix-vector product between this operator and $|\tilde{\psi}_n(t)\rangle$ proceeds along the following stages:

1. For each ion (I) and its set of projectors (j), compute the coefficients $\langle\tilde{p}_j^I|\tilde{\psi}_n(t)\rangle$
2. Effect the contribution from the local potential in $\tilde{\mathcal{H}}_{KS}$ using a real-space representation of $|\tilde{\psi}_n(t)\rangle$.
3. Effect the contribution from the non-local potential in $\tilde{\mathcal{H}}_{KS}$ and the non-local portion of $\mathcal{S}$ using the inner products computed in Step 1.
4. Effect the contribution of the kinetic energy term in $\tilde{\mathcal{H}}_{KS}$ and the identity term in $\mathcal{S}$ using a reciprocal-space representation of $|\tilde{\psi}_n(t)\rangle$.
5. Add all terms together with the appropriate weights.

A.1.2 Adding Ionic Motion

Unlike the operators in the previous section, $\mathcal{P}$ is a purely non-local operator. For convenience, we recall its definition from Equation 2.6 and the definition of the $\mathcal{T}$ operator from Equation 2.1:

$$\mathcal{P} = -i\mathcal{T}^\dagger \frac{d\mathcal{T}}{dt} \tag{A.1a}$$

$$\mathcal{T} = 1 + \sum_I \sum_j \left(|\phi_j^I\rangle - |\tilde{\phi}_j^I\rangle \right) \langle \tilde{p}_j^I| \tag{A.1b}$$

Here, the time-dependence of the $\mathcal{T}$ operator is implicit in the dependence of the partial waves and projectors on the ionic positions, $\mathbf{R}_I$ which are functions of time. Applying the chain rule, we render $\mathcal{P}$ in terms of derivatives with respect to these positions:

$$\mathcal{P} = -i \sum_I \dot{\mathbf{R}}_I \cdot \mathcal{D}_I \tag{A.2a}$$

$$\mathcal{P} = -i \sum_I \dot{\mathbf{R}}_I \cdot \sum_{j_1,j_2} \left(|\tilde{p}_{j_1}^I\rangle Q_{j_1 j_2}^I \frac{\partial \langle \tilde{p}_{j_2}^I|}{\partial \mathbf{R}_I} + |\tilde{p}_{j_1}^I\rangle \left[\langle \phi_{j_1}^I | \frac{\partial \phi_{j_2}^I}{\partial \mathbf{R}_I} \rangle - \langle \tilde{\phi}_{j_1}^I | \frac{\partial \tilde{\phi}_{j_2}^I}{\partial \mathbf{R}_I} \rangle \right] \langle \tilde{p}_{j_2}^I| \right) \tag{A.2b}$$

Here, we have introduced $Q_{j_1 j_2}^I$, the details of which are discussed in [22]. We consider the calculation of the projector derivative/first term and the partial wave derivative/second term separately.

The $\mathbf{R}_I$-dependence of the projector is very simple in the plane wave basis:

$$|\tilde{p}_j^I\rangle = \sum_{\mathbf{G}} \tilde{p}_j^I(\mathbf{G}) e^{i\mathbf{G}\cdot\mathbf{R}_I} |\mathbf{G}\rangle \tag{A.3}$$

To this end, the first term in parentheses in Equation A.2b can be rendered as:

$$-\sum_I \sum_{\mathbf{G}} \dot{\mathbf{R}}_I \cdot \mathbf{G} |\mathbf{G}\rangle \left(\sum_{j_1 j_2} \tilde{p}_{j_1}^I(\mathbf{G}) Q_{j_1 j_2}^I \overline{\tilde{p}_{j_2}^I(\mathbf{G})} \right) \langle \mathbf{G}| \tag{A.4}$$

The partial wave derivative is slightly more difficult to consider. In real-space, the AE partial wave terms have the following form:

$$\phi_{j_1}^I(\mathbf{r}) = g_{j_1}^I(|\mathbf{r} - \mathbf{R}_I|) Y_{j_1}(\theta_I, \phi_I) \tag{A.5}$$

That is, a product of a radial function centered about the Ith ion and a spherical harmonic in terms of angular coordinates defined about the Ith ion. The PS partial wave takes the same form. Because these functions only depend upon $\mathbf{r} - \mathbf{R}_I = \tilde{\mathbf{r}}^I$, we can make the identification $\frac{\partial}{\partial \mathbf{R}_I} \to -\frac{\partial}{\partial \tilde{\mathbf{r}}_I}$. Using this, we can write the AE integral in the partial wave derivative term as:

$$\langle \phi_{j_1}^I | \frac{\partial \phi_{j_2}^I}{\partial \mathbf{R}_I} \rangle = -\int \tilde{r}_I^2 \sin(\theta) dr_I d\theta d\phi \; g_{j_1}^I(\tilde{r}_I) Y_{j_1}(\theta_I, \phi_I) \frac{\partial}{\partial \tilde{\mathbf{r}}_I} g_{j_2}^I(\tilde{r}_I) Y_{j_2}(\theta_I, \phi_I) \tag{A.6}$$

These integrals can then be computed by quadrature.

A.1.3 Applying an Impulsive Field

We consider the evaluation of initial conditions for optical response calculations described in Equation 4.2. It is evident that resolving the initial conditions requires the solution of a linear system of equations. Other authors have previously noted that dropping all forms of the $\mathcal{T}$ operator from the above Equation allow the initial conditions to be determined by simply applying the phase factor to the ground state KS wavefunctions [31]. In so far as this initial step is relatively inexpensive, and it guarantees that the initial kets are normalized in the $\mathcal{S}$-weighted norm, we have implemented the proper solution of Equation A.7.

Implementation is simpler if we first apply $\mathcal{T}^\dagger$ to both sides of Equation 4.2a.

$$\mathcal{S}|\tilde{\psi}_n(t=0^+)\rangle = \mathcal{T}^\dagger e^{i\mathbf{A}_0\cdot\hat{\mathbf{r}}}\mathcal{T}|\tilde{\psi}_n^0\rangle \tag{A.7}$$

The same CGS solver used for the Crank-Nicolson update will be applied with $\mathcal{S}$ on the LHS, rather than the matrices described in Appendix A.1.1. The remaining problem then becomes the evaluation of the RHS ket. Following the usual prescription for constructing the PAW form of a local operator, the operator producing the RHS can be rendered as:

$$\mathcal{T}^\dagger e^{i\mathbf{A}_0\cdot\hat{\mathbf{r}}}\mathcal{T} = e^{i\mathbf{A}_0\cdot\hat{\mathbf{r}}} + \sum_I \sum_{j_1,j_2} |\tilde{p}_{j_1}^I\rangle \left[\langle\phi_{j_1}^I|e^{i\mathbf{A}_0\cdot\hat{\mathbf{r}}}|\phi_{j_2}^I\rangle - \langle\tilde{\phi}_{j_1}^I|e^{i\mathbf{A}_0\cdot\hat{\mathbf{r}}}|\tilde{\phi}_{j_2}^I\rangle\right]\langle\tilde{p}_{j_2}^I| \tag{A.8}$$

The first term can be applied trivially after transforming the target ket into real-space, and the remaining non-local term can be applied easily in reciprocal-space, assuming knowledge of the matrix elements enclosed in square brackets. These matrix elements take the form:

$$\tilde{Q}_{j_1,j_2}^I(\mathbf{A}_0) = \int d\mathbf{r}\; g_{j_1}^I(\tilde{r}_I)Y_{j_1}(\theta_I,\phi_I)g_{j_2}^I(\tilde{r}_I)Y_{j_2}(\theta_I,\phi_I)e^{i\mathbf{A}_0\cdot\hat{\mathbf{r}}} \tag{A.9}$$

Here, the expansion of the phase factor in terms of atom-centered spherical harmonics yields the following factorized form of the matrix elements:

$$\tilde{Q}_{j_1,j_2}^I(\mathbf{A}_0) = e^{i\mathbf{A}_0\cdot\mathbf{R}_I}\sum_L^\infty 4\pi(i)^L\left(\int d\tilde{r}_I\;\tilde{r}_I^2 g_{j_1}^I(\tilde{r}_I)g_{j_2}^I(\tilde{r}_I)j_L(A_0\tilde{r}_I)\right)\times$$
$$\sum_{M=-L}^L Y_{L,M}(\theta_{A_0},\phi_{A_0})\int d\theta_I d\phi_I\;\sin(\theta_I)Y_{L,M}(\theta_I,\phi_I)Y_{j_1}(\theta_I,\phi_I)Y_{j_2}(\theta_I,\phi_I) \tag{A.10}$$

The integral of the product of three spherical harmonics is a well-known quantity [42] which naturally truncates the infinite sum in L, and the finite set of radial integrals are performed numerically.

A.2 Calculation of Bulk Optical Response

In contrast to the finite systems approach in Chapter 4, when considering extended systems the effect of long-range polarization must be taken into account when computing

the optical response. Bertsch, et. al. [41] were the first to present the necessary modification to real-time TDDFT to capture this physics. Here, we provide a brief overview of their approach and details germane to its implementation.

We will consider the evolution of the KS state under the action of Equation 2.4 in the limit of immobile ions and adding an external time-dependent electric field to the KS Hamiltonian, as in Chapter 4. To this end, we will consider the same initial conditions as in Equation 4.2. However, rather than considering the system's dipole moment, we will instead look at the TD surface charge that is induced by the initial perturbation, the dynamics of which will yield information concerning the bulk dielectric function. This surface charge will simply appear as an induced contribution in the total vector potential, $\mathbf{A}(t)$, which will remain uniform over the entire system. With this in mind, the following extensions must be made:

- As the vector potential is no longer a constant, it must be included in the TDKS Hamiltonian.
- Separate classical equations of motion must be evolved for the total vector potential in conjunction with the TDKS equations.
- The TD electric field arising from the total vector potential must be retained to compute the system dielectric function.

Inclusion of the vector potential into $\tilde{\mathcal{H}}_{KS}$ is relatively simple. The kinetic energy term must be modified in the usual way, $\mathbf{p} \to \mathbf{p} - \mathbf{A}(t)$, and a gauge transformation must be applied to the nonlocal contribution to the potential to preserve gauge invariance of $\tilde{\mathcal{H}}_{KS}$. Calculation of the modified terms is straight forward in the basis of plane waves, in which the $\mathbf{p} \cdot \mathbf{A}(t)$ and $|\mathbf{A}(t)|^2$ terms are diagonal.

The equations of motion for $\mathbf{A}(t)$ take the form of a 2nd order ODE:

$$\left(\frac{d^2}{dt^2} + \omega_p^2\right) \mathbf{A}(t) = \mathbf{j}_{KS}(t) + \mathbf{j}_{PAW}(t) = \mathbf{j}_{RHS}(t) \tag{A.11}$$

Here, ω_p^2 is the plasmon frequency associated with the non-frozen electrons, $\mathbf{j}_{KS}(t)$ is the current density at the system boundary, and $\mathbf{j}_{PAW}(t)$ arises from the gauging of the nonlocal part of the potential. The numerical integration of this ODE with the TDKS equations is achieved using a Verlet integrator for $\mathbf{A}(t)$ outside of the Crank-Nicolson integrator established in Chapter 2. Integration proceeds as follows:

1. Update $\mathbf{E}(t) = -\frac{d\mathbf{A}}{dt}$: $\mathbf{E}(t + \frac{\Delta t}{2}) = \mathbf{E}(t) + \frac{\Delta t}{2}\left(\mathbf{A}(t) - \mathbf{j}_{RHS}(t)\right)$.
2. Update the KS orbitals using the full Crank-Nicolson integrator from time t to $t + \Delta t$, using $\mathbf{A}(t)$ in $\tilde{\mathcal{H}}_{KS}$.
3. Update $\mathbf{A}(t)$: $\mathbf{A}(t + \Delta t) = \mathbf{A}(t) + \Delta t \mathbf{E}(t + \frac{\Delta t}{2})$.
4. Update $\mathbf{E}(t + \frac{\Delta t}{2})$: $\mathbf{E}(t + \Delta t) = \mathbf{E}(t + \frac{\Delta t}{2}) + \frac{\Delta t}{2}\left(\mathbf{A}(t + \Delta t) - \mathbf{j}_{RHS}(t)\right)$

Similar to the dipole response in Chapter 4, the Fourier spectrum of $\mathbf{E}(t)$ is the observable

quantity of interest. Here, we find that the system dielectric function can be computed from:

$$\frac{1}{\varepsilon_{\alpha\beta}(\omega)} = 1 - \frac{1}{A_\beta(0)} \int_0^{T_{sim}} dt\ e^{i\omega t} w(t) E_\beta(t) \tag{A.12}$$

As before, $w(t)$ is a windowing function that ensures that the integrand goes smoothly to 0 for $t \geq T_{sim}$. Here $\mathbf{A}(0)$ and $\mathbf{E}(t)$ have been written in component form to emphasize that this method is capable of resolving even anisotropic dielectric functions, albeit, requiring 3 independent calculations.

DISTRIBUTION:

1 Attn: G. Bertsch
Department of Physics, Box 351560
University of Washington
Seattle, WA 98195, USA

1 Attn: A. Correa
Lawrence Livermore National Laboratory
7000 East Avenue, L-413
Livermore, CA 94550, USA

1 Attn: F. Graziani
Lawrence Livermore National Laboratory
P.O. Box 808
Livermore, CA 94551

1 Attn: E.K.U Gross
Max Planck Institute of Microstructure Physics
Weinberg 2
Halle (Saale) 06120, Germany

1 Attn: J. Kress
Theoretical Division, Mail Stop B268
Los Alamos National Laboratory
Los Alamos, NM 87545, USA

1 Attn: N. Maitra
Department of Physics and Astronomy
Hunter College and the City University of New York
695 Park Ave. Room 1214E North Building
New York, NY 10065, USA

1 Attn: J. Rehr
Department of Physics, Box 351560
University of Washington
Seattle, WA 98195, USA

1 Attn: A. Schleife
Department of Materials Science and Engineering
University of Illinois at Urbana-Champaign
1304 W. Green St.
Urbana, IL 61801, USA

1 Attn: E. Schwegler
Lawrence Livermore National Laboratory
7000 East Avenue, L-413
Livermore, CA 94550, USA

1 Attn: K. Yabana
Center for Computational Sciences
University of Tsukuba
Tsukuba 305-8577, Japan

1	MS 1179	H. Hjalmarson, 1341
1	MS 1189	D. Flicker, 1640
1	MS 1189	T. Mattsson, 1641
1	MS 1315	N. Modine, 1131
1	MS 1322	P. Schultz, 1425
1	MS 1415	A. Wright, 1131
1	MS 0899	Technical Library, 9536 (electronic copy)
1	MS 0359	D. Chavez, LDRD Office, 1911

Sandia National Laboratories